Label-Free Imaging of Cancer Stem Cells and Glioblastoma Grading Using Mannose-weighted CEST MRI

Behnaz Ghaemi, PhD [1,2], Hernando Lopez-Bertoni, PhD [3,4], Shreyas Kuddannaya, PhD[1,2], John J. Laterra, MD, PhD[3,4], Guanshu Liu, PhD [1,5], Jeff W.M. Bulte, PhD [1-3,5]

[1]Russell H. Morgan Department of Radiology and Radiological Science, Division of MR Research, [2]Cellular Imaging Section and Vascular Biology Program, Institute for Cell Engineering, [3]Department of Oncology, [4]Department of Neurology, the Johns Hopkins University School of Medicine, Baltimore, Maryland, USA. [5]F.M. Kirby Research Center for Functional Brain Imaging, Kennedy Krieger Inc., Baltimore, Maryland, USA.

Introduction: Glioblastoma is one of the most aggressive cancers known to men. Non-invasive assessment of aggressiveness is crucial for treatment planning, but current MRI protocols lack specificity. Amide proton transfer CEST MRI can grade diffuse gliomas, but not GBM aggression levels. GBM invasiveness arises from a shift from a pro-neural to mesenchymal phenotype. Based on a report that mannose-weighted (MANw) CEST MRI can be used for detection of unlabeled mesenchymal stem cells overexpressing mannose [1], we investigated if mesenchymal cancer stem cells could be detected "label-free" in a similar fashion.

Materials and Methods: Low aggressive GBM1a and highly aggressive M1123 cells were used throughout. Mannose expression was assessed using fluorescein-labeled galanthus nivalis lectin (GNL-FITC, specific for mannose) staining, and the mesenchymal cellular phenotype by anti-CD44 immunostaining. In vitro MANw CEST MRI was conducted using a Bruker 11.7T vertical bore spectrometer. Z-spectral data were collected using a CW RF pulse of B_1=2.4 μT, and T_{sat}=3 s. For in vivo tumor models, 2×10^5 M1123 and GBM1a spheres were injected into the right and left striatum of NSG mice brain. In vivo T2-w and MANw CEST MRI was performed 1, 8 and 16 days after injection using an 11.7 T Bruker Biospin horizontal bore scanner. CEST MRI was performed with a saturation pulse B_1=2.4 μT and T_{sat}=3 s, with the saturation frequency step between ±5 ppm. Tumor and brain ROIs were manually drawn based on T2-w images. For M1123 cells, the mannose-binding lectins LMAN1 and LMAN2 were knocked down using liposomal transfection with LMAN 1/2 siRNA, and LMAN1/2 expression was quantified with qRT-PCR and normalized to GAPDH. Subsequently, the MANw CEST signal in the KD group was compared with the control both in vitro and in vivo.

Results and Discussion: GNL staining indicated low mannose expression for both 2D cell cultures, but M1123 3D sphere cultures contained more mannose (MCSCs) compared to GBM1a. In vitro MANw CEST MRI showed the highest CEST signal for the M1123 3D spheres. After transplantation of 3D tumor spheres in mouse brain. T2-w MRI showed M1123 cells growing much faster than GBM1a invading across the entire hemisphere on day 16, with pronounced hypointense regions due to necrosis and hemorrhage. For the MANw CEST MRI on day 1, a distinct signal was observed for M1123, whereas GBM1a signal levels were not distinguishable from normal brain tissue background. Eight and 16-day post-injection follow-up revealed a continuous pronounced MANw CEST signal only for the highly aggressive tumor, with an excellent correlation for anti-mannose staining. The difference in MANw CEST signal of M1123 was significantly higher (>1.8-fold) than GBM1a and host brain for all three time points. Anti-CD44 immunostaining revealed an abundance of mesenchymal cells in the M1123 tumor, but none in the GBM1a. Moreover, the highest density was found in the periphery of the M1223 tumor mass, representing the most malignant, outwards growing mesenchymal cancer stem cells. Silencing LMAN1/2 in M1223 cells resulted in a 4-fold reduction of LMAN1/2 expression and mannose glycosylation, which was accompanied by a ~10% reduction in MANw CEST MRI contrast in vitro. In vivo results demonstrated the absence of the MAN signal and subsequent lack of tumor development following the transplantation of M1123 KD tumor spheres into the brain, compared to the M1123 control. This underscores the crucial role of MAN-overexpressing MCSCs in tumor development and suggests novel diagnostic and therapeutic approaches that could potentially revolutionize the treatment of aggressive GBM.

Conclusions: Highly aggressive GBM cancer stem cells overexpress mannose and exhibit a mesenchymal ($CD44^+$) phenotype. Knocking down mannose binding lectins resulted in lower mannose expression and a concomitant lower MANw CEST contrast, proving causation of CEST MRI signal and cancer stem cell phenotype instead of a mere correlation. MANw CEST MRI may allow a label-free, non-invasive diagnosis of low-to high grade malignant progression. IRB approval and clinical testing can be fast since brain tumor patients already undergo routine MRI. Once translated, this advance has the potential to improve and expedite therapeutic decisions, hopefully increasing patient survival.

References [1] Yuan, Y., et al., In vivo tracking of unlabeled mesenchymal stromal cells by mannose-weighted chemical exchange saturation transfer MRI. Nat. Biomed. Eng., 2022. 6(5): p. 658-666.

Impact of isoflurane anesthesia on brain metabolism in mice: calibration and validation with EEG

Zhiliang Wei, PhD[1,2,#], Seung-Eon Roh, PhD[3,#], Xiuli Yang, MD, PhD[4], Wenshen Wang, PhD[1,2], Jiekang Wang, BS[5], Lin Chen, PhD[2], Yuguo Li, PhD[1,2], Adnan Bibic, PhD[2], Hanzhang Lu, PhD[1,2,5]

[1]Department of Radiology, Johns Hopkins School of Medicine, Baltimore, MD. [2]F. M. Kirby Research Center, Kennedy Krieger Research Institute, Baltimore, MD. [3]Department of Neuroscience, Johns Hopkins School of medicine, Baltimore, MD. [4]Department of Neurology, Johns Hopkins School of Medicine, Baltimore, MD. [5]Department of Biomedical Engineering, Johns Hopkins School of Medicine, Baltimore, MD. [#]These authors contributed equally to this work.

Background: Isoflurane is one of the most widely used anesthetic agents in rodent imaging studies and has been known to affect the *in-vivo* measurements of brain metabolism.

Objective: We aim to provide a method to calibrate the impact of isoflurane on brain metabolism measurements.

Methods: Non-contrast techniques of TRUST[1] and PC[2] MRI were employed to dynamically measure the cerebral metabolic rate of oxygen ($CMRO_2$) under varying doses of isoflurane anesthesia in mice (Figure 1A; N=8 mice). Experimental parameters followed the reported protocols.[1,2] Concurrently, systemic parameters of heart and respiration rates were recorded alongside $CMRO_2$. For validation, electroencephalogram (EEG)[3] recording was used to identify changes in neuronal activities under the same anesthetic regimen employed in the MRI experiments (N=6 mice).

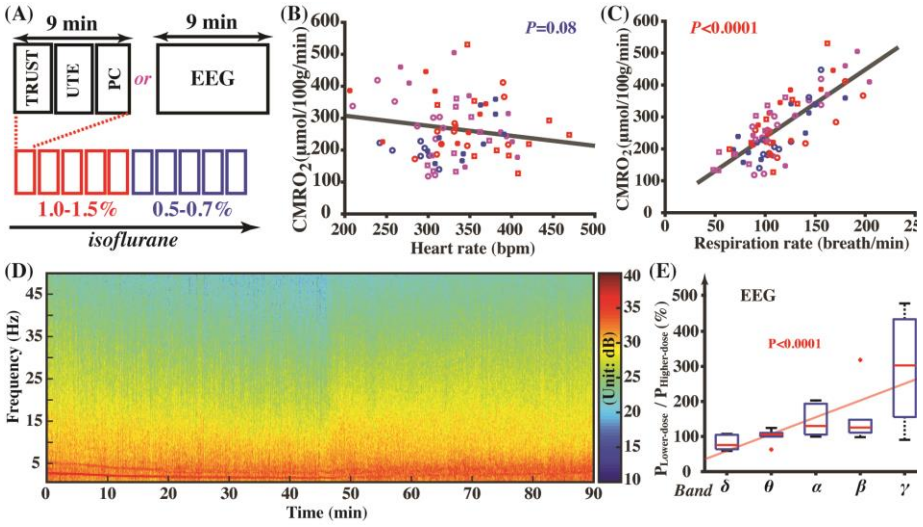

Figure 1 Calibration of metabolism measurements under isoflurane in mice. (A) schematic diagram of experimental design; TRUST: T2-relaxation-under-spin-tagging; PC: phase-contrast; UTE: ultrashort TE; EEG: electro-encephalogram. (B) correlation between heart rate and $CMRO_2$ (N=8). (C) correlation between respiration rate and $CMRO_2$; (D) averaged spectral power density heatmap (N=6). (E) dependence of normalized EEG power on the frequency bands. δ: 0.5-4Hz; θ: 4-8Hz; α: 8-12Hz; β: 12-30Hz; γ: 30-50Hz.

Results: Over the 10 recording dynamics, we found that $CMRO_2$ and respiration rate exhibited time-dependent increases (linear regression: P<0.0001), and heart rate showed a significant decrease (P=0.013) (data not shown due to page limit). Moreover, there was a significant correlation between $CMRO_2$ and respiration rate (slope = 2.117 μmol/100g/breath, CI = [1.726, 2.507], P<0.0001, Figure 1C), but not between $CMRO_2$ and heart rate (slope = -0.312 μmol/100g/beat, CI = [-0.663, 0.038], P=0.08, Figure 1B). Accordingly, we obtained an empirical equation to describe the quantitative relationship between $CMRO_2$ and respiration rate, $CMRO_2 = 24.750 + 2.117RR$, with a correlation coefficient of 0.77 (R = 0.77).

In the averaged spectral power density heatmap of EEG (Figure 1D), the power distributions at higher and lower doses (0-45 min *vs.* 45-90 min) were visually different, especially at the high frequency ranges. Quantitative analyses were performed using the last two blocks of the 9-min EEG data sets from each of the higher and lower dose periods, which are expected to reflect steady-state values (Figure 6B). Linear mixed effect model revealed that there was a significant frequency effect on the fractional EEG power (slope = 5.356 %/Hz, CI = [3.443, 7.269], P<0.0001, Figure 6C). Collectively, it could be inferred that the increased brain metabolism after switching to lower isoflurane doses was associated with increased brain activities at higher frequencies.

Conclusions: We have cross-validated MRI-based metabolism measurements with EEG recording. An empirical calibration scheme by reference to respiration rate is obtained for metabolism measurement, which may promisingly promote the utilization of brain metabolism in future pathophysiological studies with mouse models.

References: 1. Wei Z *et al.* Magn Reson Med (2018) 80: 521-528. 2. Wei Z *et al.* Magn Reson Med (2019) 81: 2566-2575. 3. Roh SE *et al.* bioRxiv (2023) doi: 10.1101/2023.09.26.559408.

In vivo Metabolic Sensing of Hyperpolarized [1-^{13}C]-Pyruvate in Mice Using a Recyclable Perfluorinated Iridium Signal Amplification by Reversible Exchange Catalyst

Dr. Jessica Ettedgui,*[a] Dr. Kazutoshi Yamamoto,[b] Prof. Dr. Eduard Y. Chekmenev,[c] Prof. Dr. Boyd M. Goodson,[d] Dr. Murali C. Krishna,[b] Dr. Rolf E. Swenson[a]

[a] Chemistry and Synthesis Center, National Heart, Lung, and Blood Institute, Rockville, MD 20850, United States
[b] Center for Cancer Research, National Cancer Institute, Bethesda, MD 20814, United States
[c] Department of Chemistry, Karmanos Cancer Institute (KCI), Wayne State University, Detroit, MI 48202, United States
[d] School of Chemical & Biomolecular Sciences, Southern Illinois University, Carbondale, IL 62901, United States

▪ Background

Real-time visualization of metabolic processes in vivo provides crucial insights into conditions like cancer and metabolic disorders. Metabolic magnetic resonance imaging (m-MRI), by amplifying the signal of pyruvate molecules through hyperpolarization, enables non-invasive monitoring of metabolic fluxes, aiding in understanding disease progression and treatment response. Signal Amplification By Reversible Exchange (SABRE) presents a simpler, cost-effective alternative to dissolution dynamic nuclear polarization (d-DNP), eliminating the need for expensive equipment and complex procedures.

▪ Objective

To mitigate the iridium contamination and toxicity challenge in the SABRE technique, we introduced a novel perfluorinated catalyst.[1] This catalyst exhibited high hydrophobicity and demonstrated retained polarization properties in methanol (compared to its non-fluorinated variant). Additionally, it could be removed from an aqueous solution of HP [1-^{13}C]-pyruvate using the ReD-SABRE protocol[1] with an iridium residual content of 177 ppb, the lowest reported to date for [1-^{13}C]-pyruvate and safe to use in a clinical setup.

▪ Methods

In order to further explore this novel perfluorinated SABRE catalyst, we performed hyperpolarization in a mixture of methanol and a hydrofluoroether (HFE) solvent and showed ^{13}C polarization increase to up to 16% with DMSO as a co-ligand. This 25% increase was due to the improved parahydrogen solubility in this solvent mixture. We also explored whether aqueous pyruvate could be obtained by extraction of the perfluorinated/methanol mixture.

▪ Results

The perfluorinated catalyst exhibits recyclability, maintaining its activity through subsequent [1-^{13}C]pyruvate hyperpolarization cycles. The catalyst shows no loss in activity after the two first cycles and a 30% decrease after the third cycle. Remarkably, it remains active for at least 10 cycles, albeit at a 70% loss in hyperpolarization potency and despite no automation was employed.
In addition, we present the first in vivo demonstration of metabolic sensing in a human pancreatic cancer xenograft model compared to healthy mice.

▪ Conclusions

Efficient SABRE-SHEATH hyperpolarization for production of biocompatible aqueous solutions of HP [1-^{13}C]-pyruvate with minimal iridium contamination using the perfluorinated catalyst, which also allows a 1.2-fold greater P_{13C} when using fluorinated solvents. The integrity of the catalyst‘s functionality across multiple iterations remains intact, as demonstrated by the repetitive hyperpolarization and extraction cycles of HP [1-^{13}C]-pyruvate. Given the clinical dose requirement of HP [1-^{13}C]-pyruvate, SABRE catalyst recycling becomes imperative to mitigate costs, particularly as clinical-scale production may necessitate large quantities of iridium. The findings from the in vivo study demonstrated the effectiveness of using SABRE-SHEATH polarized pyruvate in fluorinated solvents for metabolic sensing in MIA PaCa-2 xenograft tumors, affirming its capability to monitor the dynamic metabolic processes occurring within both healthy and pathological tissues in living organisms. This marks the first application of SABRE-SHEATH hyperpolarization techniques for detecting dynamically altered in vivo metabolisms within a disease model. This combination of low iridium content and catalyst recycling potentially allows SABRE to transition for routine low-cost clinical use. SABRE-SHEATH utilizing the perfluorinated SABRE catalyst emerges as an appealing, cost-effective alternative to d-DNP for preparing bio-compatible HP [1-^{13}C]-pyruvate formulations in next-generation molecular imaging.

References: 1. *Angewandte* **2024**, DOI: 10.1002/202407349; **2:** *J. Am. Chem. Soc*. **2024**, *146*, 946−953; **3.** *ACS Sens*. **2022**, *7*, 3430−3439.

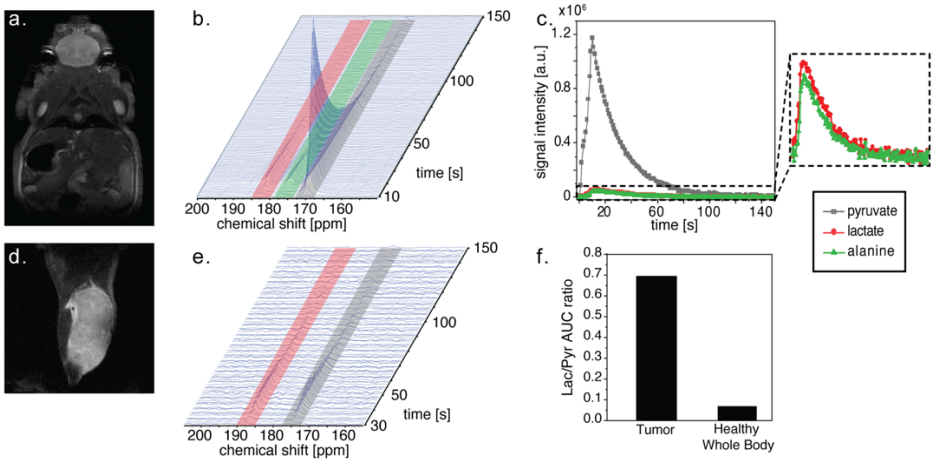

Figure 1. SABRE-SHEATH hyperpolarization of [1-^{13}C]-pyruvate sensitively detects site specific metabolism in vivo (a) T_2-weighted ^{1}H MRI of the body mouse's body. (b) Dynamic hyperpolarized ^{13}C-MR spectroscopy demonstrated in the whole body of a healthy mouse after hyperpolarized [1-^{13}C]-pyruvate injection using a whole-body detection coil. (c) Time-dependent metabolic spectroscopy of [1-^{13}C] pyruvate (grey) can depict enzymatic conversions into [1-^{13}C] lactate (red) and [1-^{13}C] alanine (green). Inset: The time-dependent metabolism of [1-^{13}C]pyruvate via enzymatic conversion into [1-^{13}C]lactate and [1-^{13}C]alanine observed in the whole-body spectroscopy. (d) T_2-weighted ^{1}H MRI of the xenografts embedded MIA PaCa-2 tumor cell lines into the right hind legs of athymic nude mice using a 17 mm diameter home-built ^{13}C solenoid coil with a saddle ^{1}H coil. (e). Aberrant in vivo metabolism in the tumor region was observed via hyperpolarized ^{13}C dynamic spectra mouse leg xenografts of MIA PaCa-2. (f) The lactate to pyruvate AUC (Area Under the Curve) ratios in the tumor regions and the whole healthy mouse body. The spectra were acquired every 1 s for 300 s on a 3T MRI scanner. [1-^{13}C]-pyruvate peak (170 ppm) was observed as well as its conversion into lactate (185 ppm). Dynamic ^{13}C MRS were processed on MATLAB with a home-made script utilizing a singular value decomposition based low rank denoising method.

Isolation and Characterization of Anti-BSG Nanobody to Target Hepatocellular Carcinoma

Divya Nambiar, BS[1], Thomas J. Esparza, BS[2], Woonghee Lee, PhD[1], Joon-Yong Chung, PhD[1], Julia Sheehan-Klenk, BA[1], Peter L. Choyke, MD[1], Freddy E. Escorcia, MD, PhD[1]

[1]National Cancer Institute, Bethesda, MD, [2]National Institute of Mental Health, Bethesda, MD

Background: Primary liver cancer is the third leading cause of cancer-related deaths worldwide, with increasing incidence and mortality. Hepatocellular carcinoma (HCC) accounts for approximately 90% of primary liver cancer, and outcomes for most patients are poor. Unlike many cancer types, liver cancer cannot reliably be detected by ^{18}F-fluorodeoxyglucose positron emission tomography (^{18}F-FDG-PET) due to limited tumor uptake. Curiously, no HCC-selective agents are clinically approved for HCC in the United States. BSG is a transmembrane glycoprotein that is expressed in 60% of HCC, and correlates with tumor invasion, metastasis, and angiogenesis. Accordingly, radiopharmaceutical agents specific to BSG could allow for HCC-selective imaging and surveillance.

Objective: We aim to construct a novel tumor-selective radiopharmaceutical agent to more accurately surveille HCC. Specifically, we chose to use a nanobody due to its size (12-15 KDa), faster blood clearance, and superior tumor penetration when compared to conventional full-length antibodies (150 KDa).

Methods: Using standard methods, we constructed a phage display library using the B cells of a naïve llama immunized with BSG. Subsequently, immunopanning was performed against this library to BSG, and specific nanobodies were isolated, as shown in figure 1A. Enriched clones were screened by ELISA to identify high binders. Lead candidate nanobodies were then sequenced and unique clones expressed to determine yield, stability, and purity. Once identified, we performed additional biophysical characterization. Using standard methods, radiolabeling with Zr-89 was performed for in vivo assessment and PET imaging.

Results: After multiple rounds of immunopanning and characterization of binding affinities, we isolated a dominant clone, G2. Specific binding was determined by ELISA, displaying a nanomolar affinity for the nanobody against BSG, as shown in figure 1B. Orthogonal binding affinity assays including Flow Cytometry and Biolayer Interferometry similarly displayed nanomolar affinity of G2 to BSG. We successfully radiolabeled G2 with the beta-emitting isotope Zr-89 and has maintained specific binding post-labeling, as seen in figure 1C. Imaging and biodistribution studies are underway comparing tumor uptake of wildtype and BSG knockout HCC cancer cells. Additionally, we are analyzing the interactions between tumor tissue and the G2 nanobody by immunohistochemistry and cell-based saturation assays.

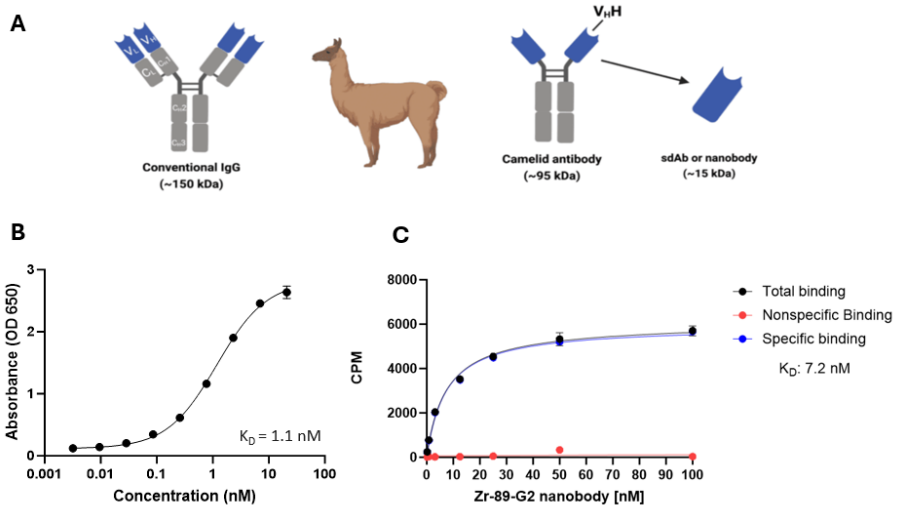

Figure 1. (A) Comparison of conventional full-length antibody to a nanobody, produced by the camelid family. (B) ELISA data shows nanomolar affinity of the G2 nanobody to BSG. (C) Cell-free Saturation Assay shows maintained binding affinity of G2 to BSG after radiolabeling.

Conclusion: We identified and have begun to rigorously characterize a unique nanobody specific to BSG. Subsequently, assessment of in vivo target binding will be performed using biodistribution studies and PET imaging.

Pharmacokinetic Profiling of Unlabeled Magnetic Nanoparticles using MPI as a Novel Cold Tracer Assay

Marzieh Salimi[1,2], Shreyas Kuddannaya[1,2], Jeff W.M. Bulte[1-6]*

[1]Russell H. Morgan Department of Radiology and Radiological Science, Division of MR Research, [2]Cellular Imaging Section and Vascular Biology Program, [3]Department of Biomedical Engineering, [4]Department of Oncology, Johns Hopkins University School of Medicine, Baltimore, Maryland, USA; [5]Department of Chemical & Biomolecular Engineering, Johns Hopkins University Whiting School of Engineering; [6]F.M. Kirby Research Center for Functional Brain Imaging, Kennedy Krieger Inc., Baltimore, MD, USA.
*Corresponding author: jwmbulte@mri.jhu.edu

Background: We present a magnetic particle imaging (MPI)-based blood assay that can be used to accurately calculate the blood half-life of magnetic nanoparticles (MNPs) without the need of labeling them. Most studies have only reported the monoexponential kinetics of MNP blood clearance (1). In only a few cases, two MNP half-lives have been reported (2-4). In this study, we report two (short and long) blood half-lives of unlabeled MNPs using MPI.
Objective: To demonstrate the feasibility and accuracy of an MPI-based blood assay for calculating the blood half-life of unlabeled MNPs and to evaluate its sensitivity in detecting MNPs in blood and tissues amidst endogenous iron presence.
Methods: Rats received 2.0 mg Fe of Synomag®-D70, Synomag®-D50, Resovist®, and Feraheme® by femoral vein injection. Blood samples were drawn from the femoral artery at various time points and their MPI relaxation signal was measured. Animals were perfused immediately following withdrawal of the 120 min blood sample. Then, liver, spleen, kidneys, stomach, heart, lungs, and mesenteric lymph nodes were harvested. PFA-fixed tissues were washed with PBS, placed in a 25 mm petri dish, and a 3D MPI scan MPI was taken using both x and z transmit axes with a gradient of 5.7 T/m, an AMF peak amplitude of 5 mT and an acquisition time of 10 min.
Results: Synomag®-D70 exhibited a biexponential blood clearance curve with half-lives of 3.2 and 31.2 min, Synomag®-D50 a monoexponential clearance with $t_{1/2}$ = 11.4 min, Resovist® a biexponential clearance with $t_{1/2}$ = 2.4 and 10.8 min, and Feraheme® a biexponential clearance with $t_{1/2}$ = 60.9 and 4.5 min (**Figure 1 A-D**). MPI quantification of iron content in tissues showed that all MNPs primarily localized in the spleen, liver, and lymph nodes, e.g., the reticuloendothelial system (**Figure 1 E**). Performed in parallel on the same samples, a Ferrozine-based spectrophotometric assay for chemical detection of MNP iron was unreliable due to the high blood and tissue iron background.
Conclusions: MPI is a sensitive and specific method capable of detecting small amounts of MNPs in blood and tissues without interference from the presence of endogenous iron. The MPI cold tracer assay is ideally suited for evaluating the in vivo pharmacokinetics of new MNP formulations and is applicable for future clinical translation.

References:

1. Yang, Hung-Wei, et al. "Self-protecting core-shell magnetic nanoparticles for targeted, traceable, long half-life delivery of BCNU to gliomas." Biomaterials 32.27 (2011): 6523-6532.
2. Bulte, Jeff WM, et al. "Initial assessment of magnetoferritin biokinetics and proton relaxation enhancement in rats." *Academic radiology* 2.10 (1995): 871-878.
3. Bulte, Jeff WM, et al. "Short-vs. long-circulating magnetoliposomes as bone marrow-seeking MR contrast agents." *Journal of Magnetic Resonance Imaging: An Official Journal of the International Society for Magnetic Resonance in Medicine* 9.2 (1999): 329-335.
4. Hamm, Bernd, et al. "Contrast-enhanced MR imaging of liver and spleen: first experience in humans with a new superparamagnetic iron oxide." *Journal of Magnetic Resonance Imaging* 4.5 (1994): 659-668.

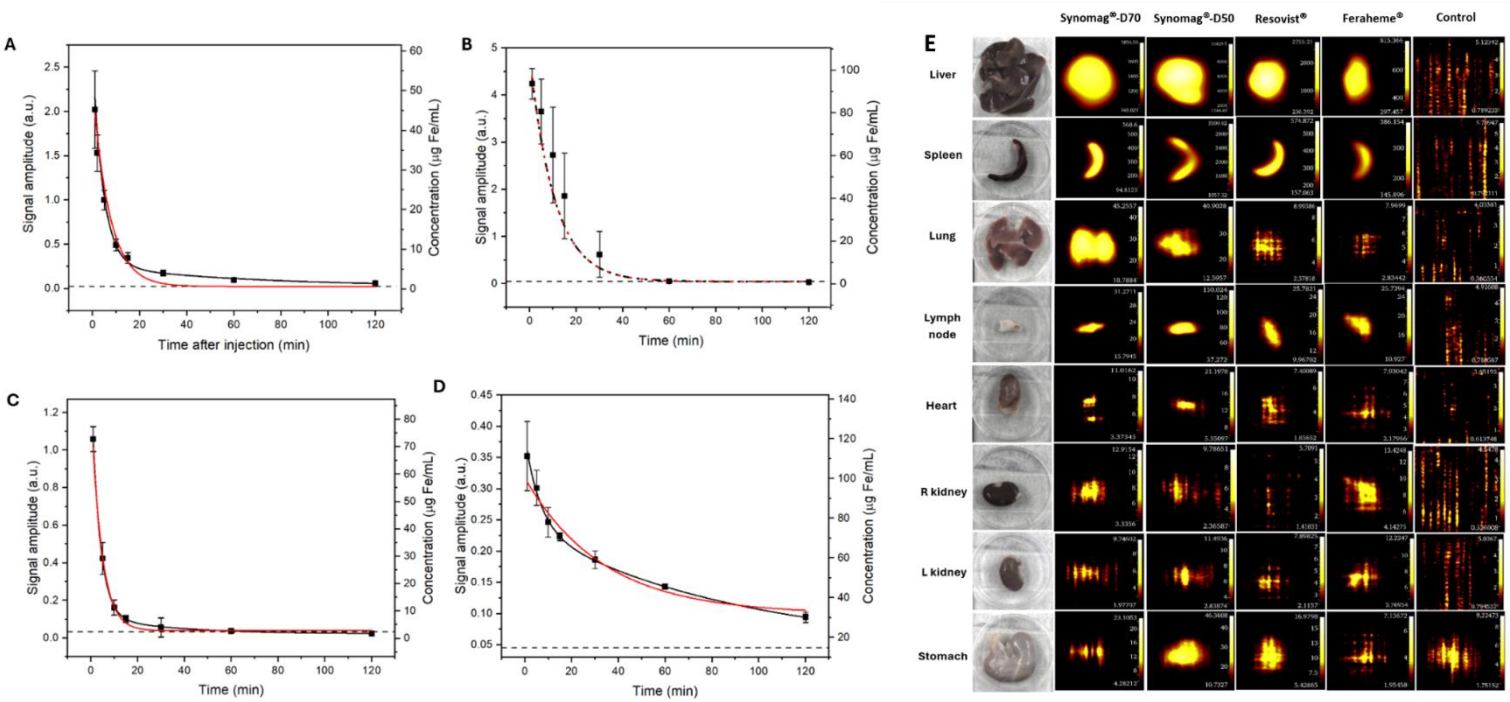

Figure 1. Measured MPI signal amplitude (left y-axis) and calculated iron concentration (right y-axis) of serial blood samples withdrawn over time after injection of 2 mg Fe/mL of **A**) Synomag®-D70, **B**) Synomag®-D50, **C**) Resovist®, and **D**) Feraheme® into the femoral vein. Dashed lines show baseline values before injection. Blood clearance curves were obtained using biexponential (black line) or monoexponential (red line) fitting, **E)** 3D MPI scans of different tissues perfused 120 min after i.v. injection of 2 mg Fe/mL of Synomag®-D70, Synomag®-D50, Resovist®, and Feraheme®.

Magnetic particle imaging for monitoring extracellular vesicle adjuvant therapy in pancreatic islet transplantation

Heng Zhao, PhD[1,2], Wenshen Wang, PhD [1,3], Olesia Gololobova, PhD [4], Geoffrey Cotin, PhD [5], Delphine Felder-Flesch, PhD [5], Guanshu Liu, PhD [3], Kenneth W. Witwer, PhD [4], Jeff W. M. Bulte PhD [1,2,6,7], Dian R. Arifin PhD [1,2]

1 Department of Radiology and Radiological Science, Johns Hopkins University School of Medicine, Baltimore, MD. 2 Cellular Imaging Section, Institute for Cell Engineering, Johns Hopkins University School of Medicine, Baltimore, MD. 3 F.M Kirby Center, Kennedy Krieger Institute, Baltimore, MD. 4 Department of Molecular and Comparative Pathobiology, Johns Hopkins University School of Medicine, Baltimore, MD. 5 SuperBranche, Strasbourg, France. 6 Department of Biomedical Engineering, Johns Hopkins University School of Medicine, Baltimore, MD. 7 Department of Oncology, Johns Hopkins University School of Medicine, Baltimore, MD.

Background: Transplantation of pancreatic insulin-producing islets has shown good potential to provide long-term and precise glucose control for juvenile diabetes patients. Short therapeutic window was encountered in islet therapy. Human mesenchymal stem cells-derived extracellular vesicles (EVs) have demonstrated the capacity to improve the survival and function of islets. One major challenge in EV therapy is the lack of ability to non-invasively elucidate EV biodistribution.

Objective: To develop a method for EV tracking using magnetic particle imaging (MPI) and superparamagnetic iron oxide nanoparticles (SuperSPIO20) as an MPI tracer.

Methods: EVs were isolated by differential centrifugation and then purified through a size exclusion chromatography (qEV) column following an established protocol.[1] EVs were labeled with hexa-histidine tagged SuperSPIO20 (Superbranche, 20 nm) using an optimized electroporation condition (300 V, 10 ms pulse, ×3), followed by Ni-NTA purification.[2] EV phantoms were imaged with a Momentum MPI scanner (Magnetic Insight, Inc.) using High Sensitivity/High Resolution mode, n=3, and sample volume=50 µL.

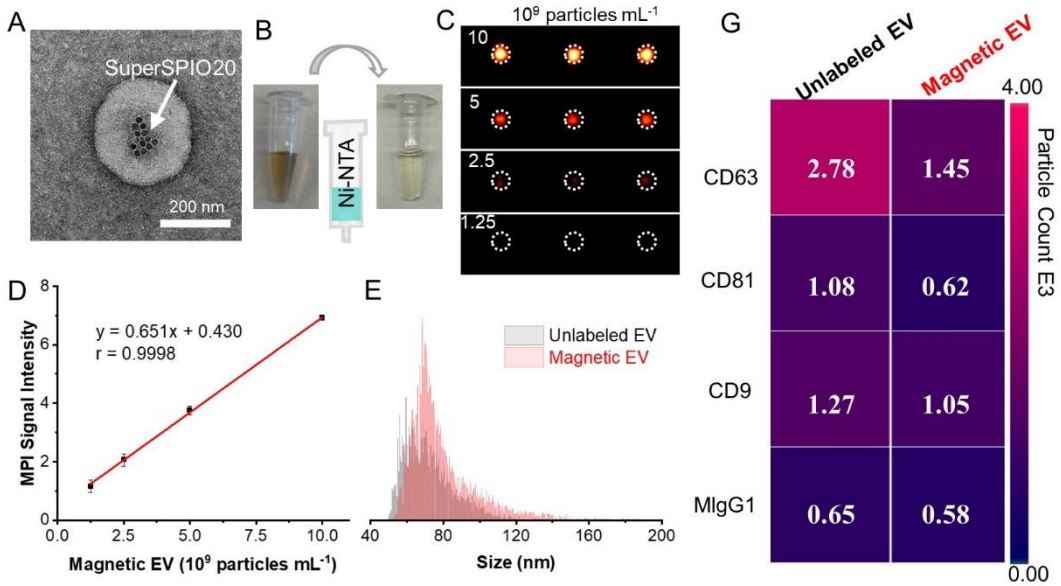

F

	Ferrozine assay (Fe/10⁹ EV)	MPI (Fe/10⁹ EV)	BCA assay (protein/10⁹ EV)
Unlabeled EV	-	-	2.5 ± 0.3 µg
Magnetic EV	1.50 ± 0.03 µg	1.62 ± 0.02 µg	1.48 ± 0.32 µg

Figure 1 (**A**) TEM of one EV encapsulating SuperSPIO20 (arrow), (**B**) EV suspension became clear after the capture of free SuperSPIO20 by an Ni-NTA column. (**C**) MPI of magnetic EVs at various concentrations and (**D**) the corresponding plot of MPI signal intensity vs. magnetic EV concentration. (**E**) NanoFCM size distribution of unlabeled and magnetic EVs. (**F**) Table of iron content as measured by Ferrozine assay and MPI, and protein content (by BCA) of unlabeled EVs and magnetic EVs. (**G**) Biomarkers (CD63, CD81 and CD9) of unlabeled EVs and magnetic EVs by nanoview. MIgG1 was the negative control.

Results: EVs have been successfully labeled by encapsulating SuperSPIO20 into the core (**Fig.1A**). Ni-NTA separated free, unencapsulated SuperSPIO20 which can give false positive signals (**Fig.1B**). MPI detected magnetic EVs as "hot spots", similar to nuclear imaging, albeit using a non-radioactive tracer (**Fig.1C**). We demonstrated a linear relationship between MPI signal intensities (SI) and magnetic EV concentration (**Fig.1D**), and agreeable iron content data from Ferrozine assay and MPI SI (**Table 1F**). EV size, size distribution, protein content and surface markers were mostly preserved post-labeling (**Fig.1E, G, Table 1F**).

Conclusion: We have shown that MPI can be used for "hot spot" passive and quantitative EV tracking without the use of radiation. Preservation of EV properties post-labeling indicated their potential for image-guided adjuvant therapy.

References: 1. Witwer KW et al., *J Extracell Vesicles* **2013,** *2, 20360*. 2. Han Z et al., *J Extracell Vesicles* **2021,** *10*, 12054.

Developing HIV broadly neutralizing antibody-producing glial progenitors to eradicate HIV from the brain.

Lorissa McDougall[1], Abdolrahim Abassi[2], Mohammad Sajadi[2], Alonso Heredia[2], Linda Chang[1], Yajie Liang[1], Chengyan Chu[1], Lukasz Kalkowski[1], Ben Atkinson[2], Miroslaw Janowski[1], Piotr Walczak[1].

[1]University of Maryland, Baltimore, Department of Radiology and Nuclear Medicine; [2]University of Maryland, Baltimore, Institute of Human Virology.

Background: Human immunodeficiency virus (HIV) affects around 1.2 million people in the U.S alone, and even though detection and treatment of this disease has progressed in the last 30 years, with the introduction of antiretroviral therapy (ART), it remains incurable. ART's can efficiently suppress HIV in peripheral blood, but, has very little impact on virus in the sanctuary sites such as brain due to being ineffective at crossing the blood brain barrier. Thus, we observe large reservoirs of infected microglial cells which allows the virus to replicate. Additionally, people with HIV (PWH) must remain on ART throughout their lifetime to ensure that these reservoirs are unable to spread back again into the body. Current limitations of ART treatments are that residual virus in the brain causes neurological deficits, and that there is an increased risk of side effects from ART over time, such as liver and kidney toxicity and changes to lipids in the GI. These side effects of ART may require interruption of treatment, resulting in re-infection throughout the body.

Objective: Our research aims to develop a therapy that utilizes the migratory abilities of glial progenitor cells by engineering them to produce an antibody neutralizing HIV. The lentiviral constructs (CII and CIII) encode a broad neutralizing antibody (bNAb) that recognizes the glycoprotein of HIV, neutralizing free virus particles and destroying HIV-expressing cells. The glial progenitor cells will be injected intra-arterially, travel to the brain, and move across the blood-brain barrier for implantation and antibody production. These cells have shown stable expression of the construct, successful binding of the bNAb to glycoprotein-120 (gp120), neutralization of HIV Pseudovirus particles, and antibody expression *in vivo*.

Methods and results: Through flow cytometry, we have identified the GFP construct-reporter and antibody co-expression in 91.6% of the CII-integrated mGRP populations and 89.9% of the CI-integrated mGRP populations. We also found, via ELISA, that CII mGRPs release an average of 3.4ug/ml of antibody into the supernatant, while CIII mGRPs release an average of 11.5ug/ml. Immunofluorescence has indicated that both the CII and CIII populations express a higher percentage of bNAb than GFP, with 7.3% of CII mGRPs expressing GFP, while 23.8% express the bNAb and 15.7% of CIII mGRPs expressing GFP, while 37.7% express the bNAb. This is due to GFP being transiently expressed as the construct is transcribed, which further indicates the stability of the antibody in our cells. We also observed that the antibody is mostly located at the cell membrane, with some also visible in the cytoplasm, indicating that these cells efficiently transport the antibody for release. In addition, the CII and CIII bNAbs have been purified and tested in a pVNT neutralization assay to determine their ability to bind the virus and thus inhibit infection, of which the CII bNAb showed >50% neutralization by 1.2ug/ml and a total 98% neutralization, while CIII showed >50% neutralization by 0.4ug/ml and a total 97% neutralization. *In vivo,* injection of the mGRP cells alongside gp120 expressing RAJI cells into the brains of NOG mice has allowed us to identify bNAb production from the mGRPs via binding to the RAJI cells. We calculated that 61.7% of cells in the needle track were bound by CII bNAb while 21.6% of cells were bound by the CIII bNAb.

Conclusions: These current findings suggest that glial progenitor cells are an appropriate model for both modification and the delivery of broad neutralizing antibodies. We are also confident that the construct design, for both CII and CIII, has successfully produced antibodies able to bind the HIV gp-120. In addition, these constructs have the potential to be altered to encode other antibodies for the recognition of different antigens. Going forward we will determine the migratory ability of the glial progenitors and thus the efficacy of delivering the therapy inter-arterially *in vivo*.

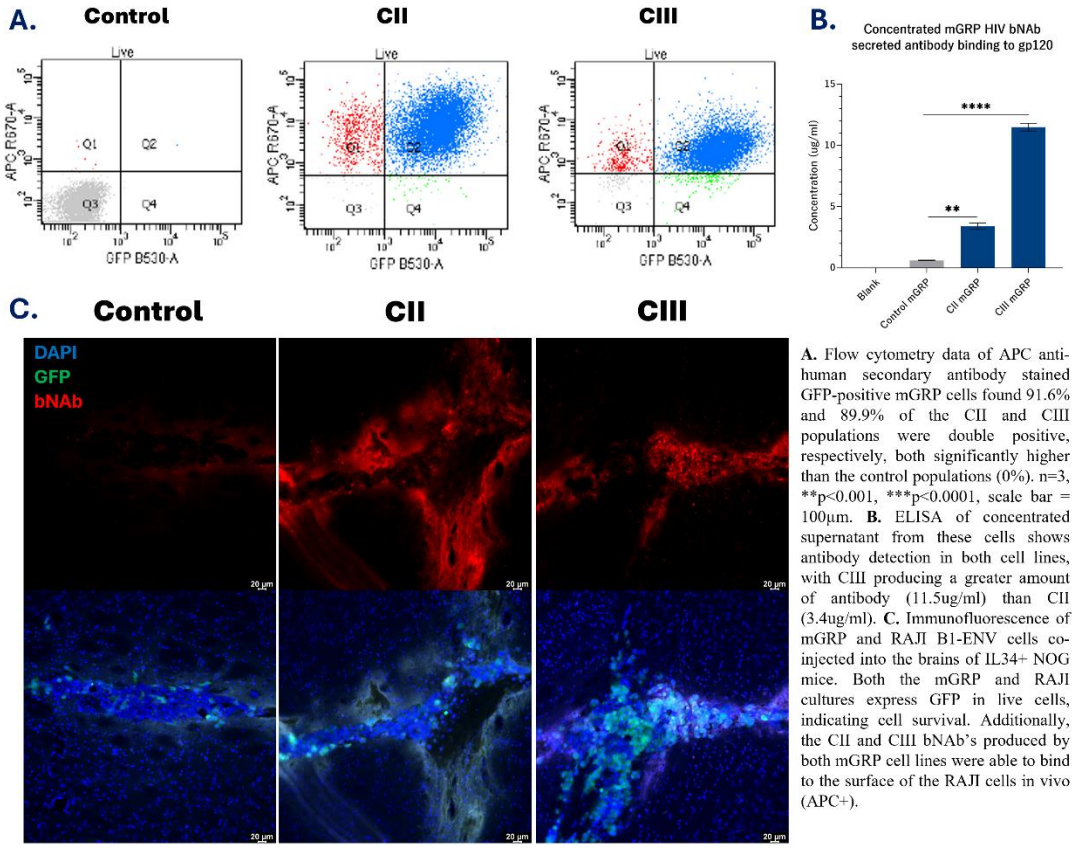

A. Flow cytometry data of APC anti-human secondary antibody stained GFP-positive mGRP cells found 91.6% and 89.9% of the CII and CIII populations were double positive, respectively, both significantly higher than the control populations (0%). n=3, **p<0.001, ***p<0.0001, scale bar = 100µm. **B.** ELISA of concentrated supernatant from these cells shows antibody detection in both cell lines, with CIII producing a greater amount of antibody (11.5ug/ml) than CII (3.4ug/ml). **C.** Immunofluorescence of mGRP and RAJI B1-ENV cells co-injected into the brains of IL34+ NOG mice. Both the mGRP and RAJI cultures express GFP in live cells, indicating cell survival. Additionally, the CII and CIII bNAb's produced by both mGRP cell lines were able to bind to the surface of the RAJI cells in vivo (APC+).

MC-Former: motion artifacts reduction in brain MRI using vision transformers and self-supervised learning

Lei Zhang, PhD, Xiaoke Wang, PhD, Edward H. Herskovits, MD, PhD, Elias R. Melhem, MD, Linda Chang, MD, Ze Wang, PhD, Thomas Ernst, PhD

Department of Diagnostic Radiology and Nuclear Medicine, University of Maryland Baltimore, USA.

Background: Motion in human subjects is inevitable and motion-induced magnetic resonance imaging (MRI) artifacts can deteriorate image quality and reduce diagnostic accuracy.

Objective: The purpose of this work is to develop and assess a motion correction method using a self-supervised learning and vision transformers named MC-Former.

Methods: Existing 3T 3D sagittal magnetization-prepared rapid gradient-echo (MP-RAGE) scans from 52 subjects were used to generate 13,700, 1,950 and 4,680 slices as training, validation, and test sets. The MC-Former was derived from a vision transformers-based model with encoder-decoder structure and skip connections. We randomly masked 50% of patches from the T1-weighted axial clean image as input and reconstructed the missing patches using self-supervised pre-training. T1-weighted axial brain images contaminated with synthetic motions were then used to train the MC-Former to remove motion artifacts. Evaluation used simulated T1-weighted axial images unseen during training. The MC-Former is compared against MC-Net[1] and Restormer[2], which are state-of-the-art methods for motion correction and motion deblurring. Performance indices included the peak signal to noise ratio (PSNR) and structural similarity index measure (SSIM). Paired t-tests were used for comparisons with p-value<0.05 considered significant.

Results: The MC-Former significantly outperformed the other two methods in terms of both PSNR and SSIM (Figure 1). In Figure 1A and 1B, the first row of each subfigure contains the "clean" (reference) image, corrupted image, and motion correction results using the MC-Net[1], Restormer[2], and the proposed MC-Former. The SSIM and PSNR values for each corrected image (relative to the "clean" image) are also shown. The second row of each subfigure zooms in on the red rectangle. The third row shows the error maps between the reference ("clean") image and corrupted and corrected images (absolute value of the difference between results and clean image multiplied 5.0). The proposed MC-Former recovers more image details than the MC-Net and Restormer; this is especially noticeable in the cerebellar region in Fig. 1A.

Conclusion: The proposed method can effectively suppress motion artifacts in brain MRI without compromising image quality. Given the effectiveness and efficiency of the proposed method, it can potentially be used in clinical settings. To facilitate further research, the code and trained model are available at https://github.com/MRIMoCo/MC-Former.

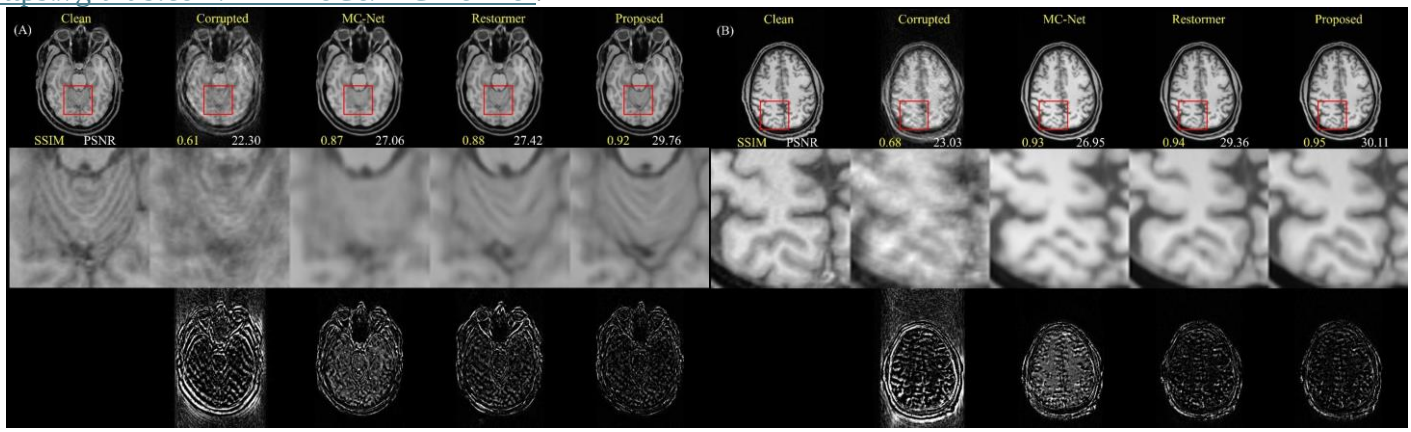

References:

1. L. Zhang *et al.*, "Motion Correction for Brain MRI Using Deep Learning and a Novel Hybrid Loss Function," *Algorithms*, vol. 17, no. 5, p. 215, 2024.

2. S. W. Zamir *et al.*, "Restormer: Efficient transformer for high-resolution image restoration," in Proceedings of the IEEE/CVF conference on computer vision and pattern recognition, 2022, pp. 5728–5739.

EphA2 targeting peptide-based radiotheranostic for pancreatic adenocarcinoma (PDAC)

Ajay Kumar Sharma Ph.D., Kuldeep Gupta Ph.D., Akhilesh Mishra Ph.D., and Sridhar Nimmagadda Ph.D.

Russell H Morgan Department of Radiology and Radiological Science, and Sidney Kimmel Comprehensive Cancer Center, Johns Hopkins University, School of Medicine, Baltimore, MD.

Background: Pancreatic ductal adenocarcinoma (PDAC) is a deadly disease and early diagnosis and therapy is paramount for effective intervention. The development of a molecularly targeted theranostic agent holds great promise in providing an early diagnosis by imaging modalities like positron emission tomography (PET). Additionally, such agents could also be used as radiotherapeutics for PDAC, potentially improving survival rates and addressing the current unmet medical need. EphA2, a member of Erythropoietin-producing hepatocellular (Eph) receptors, is a desirable target for PDAC as it is pro-oncogenic and expressed in > 90% of PDACs.

Objective: To develop an EphA2-targeting theranostic pair derived from the 14-amino-acid peptide AJ210, and to comprehensively assess its potential as a PET imaging agent and efficacy as a radiotherapeutic in xenograft and syngeneic mouse models of PDAC.

Methods: A bicyclic peptide, AJ210 was synthesized (**Figure 1A**) and binding affinity for EphA2 was determined by surface plasmon resonance (SPR). AJ210 was labelled with PET isotope Gallium-68 in high radiochemical yields and purity. In vitro uptake of the resulting [^{68}Ga]AJ210 was carried out in various human and mouse PDAC cell lines with variable EphA2 expression (Panc1, Panc02, KPC). Jurkat cell line was used as a negative control. In vivo assessment of [^{68}Ga]AJ210 was carried out by PET-CT imaging and ex vivo biodistribution studies in subcutaneous Panc1 xenografts and syngeneic KPC tumors (n=4-5/tumor). The in vivo specificity of [^{68}Ga]AJ210 for EphA2 was confirmed through cross-correlative immunohistochemistry of xenografts. Further, AJ210 was labelled with therapeutic isotope Actinium-225 in high radiochemical yield and its therapeutic efficacy was evaluated in KPC tumor bearing mice. Subsequent toxicity assessments involved evaluating hematological parameters and H&E staining of sections from vital organs.

Results: AJ210 binds human EphA2 with high affinity (K_D ~ 2 nM). Flow cytometry analysis confirmed variable EphA2 expression in the tested PDAC cell lines, with Panc1 and KPC cell lines exhibiting high levels, while panc02 and Jurkat displayed low expression. In vitro binding assays showed variable [^{68}Ga]AJ210 uptake across all PDAC cells with minimal uptake in the presence of 1 µM non-radioactive AJ210 and in negative control Jurkat cells. In vivo PET-CT imaging revealed specific and high uptake of [^{68}Ga]AJ210 in Panc1 xenografts and KPC tumors (**Figure 1B**). Notably, [^{68}Ga]AJ210 exhibited fast clearance from normal tissues resulting in high contrast images within 60 minutes. Also, evaluation of therapeutic efficacy of [^{225}Ac]AJ210 in KPC tumor model demonstrated significant reduction in tumor growth (**Figure 1C**) and improved median survival compared to saline treated animals (27 days vs 38 days, P<0.002). Furthermore, body weight monitoring, H&E staining of lungs and liver, and analysis of hematological parameters of mice treated with [^{225}Ac]AJ210 demonstrated an acceptable safety profile.

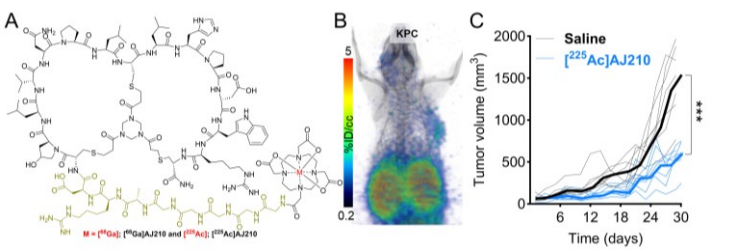

Figure 1. A) Structure of bicyclic peptide AJ210 having DOTA as bifunctional chelator for ^{68}Ga and ^{225}Ac labeling **B)** whole body static PET imaging at 60 min post injection with [^{68}Ga]AJ210 in KPC syngeneic tumor model **C)** Effect of [^{225}Ac]AJ210 (n = 7) on the KPC tumor growth (data mean ± SD) after administration of total 37 kBq via tail-vein injection

Conclusion: AJ210, a high-affinity peptide-based radiotheranostic agent specific to EphA2, serves as a powerful tool for detecting PDAC in both human and mouse models with PET. When labeled with Actinium-225, AJ210 effectively controls tumor growth. This unique combination of [^{68}Ga]AJ210-PET for imaging and [^{225}Ac]AJ210 for radiotherapy showcases the potential of AJ210 in guiding precision radiotherapeutic interventions for PDAC patients.

Advanced MRI Monitoring of Gene Expression: Evaluating rAAV-Delivered SuperCESTide for Liver Imaging

Zinia Mohanta[1,4], Aruna Singh[1,4], Julia Stabinska[1,4], Sophie Sall[2,5], Hernando Lopez Bertoni[2,5], Hilary Vernon[3], Charles P. Venditti[6], Assaf A. Gilad[7], Michael T. McMahon[1,4]

AFFILIATIONS: [1]Department of Radiology, [2]Neurology, [3]Genetics, Johns Hopkins School of Medicine; [4]F.M. Kirby Research Center for Functional Brain Imaging, [5]NeuroOncology, Kennedy Krieger Institute, Baltimore, MD, United States; [6] Metabolic Medicine Branch, National Human Genome Research Institute, National Institutes of Health (NIH), Bethesda, MD, United States; [7]Department of Chemical Engineering, Michigan State University, East Lansing, MI, United States

Introduction: For individuals with genetic disorders, viral gene delivery using recombinant adeno-associated viruses (rAAV) is becoming a viable therapeutic option. Gene addition therapy shows considerable promise, but a major challenge surrounds the in vivo monitoring of transgene expression. A practical solution is to tag the transgene with a cis-linked reporter gene. In this study, we have integrated the superCESTide reporter gene, which has been engineered to provide chemical exchange saturation transfer (CEST) MRI contrast, into an rAAV and non-invasively monitored transgene expression in the liver following systemic delivery of the vector.

Objectives: To assess the effectiveness of rAAV mediated delivery of a superCESTide reporter using a new steady-state CEST acquisition method to monitor transgene expression in vivo.

Methods: rAAV vectors were engineered to express either the superCESTide reporter gene or the control gene tdTomato, both under the enhanced chicken beta-actin promoter and pseudotyped with the AAV8 capsid. MRI studies were conducted using a Bruker Biospec 11.7 T scanner. In vivo CEST MRI data employing Proton Resonance Enhancement and Shift Exchange (PRECISE) pulse and Gaussian pulse was acquired from two groups of C57Bl/6 mice: one group expressing tdTomato (control, n=5) and another expressing both superCESTide and tdTomato (superCESTide, n=5). A steady-state saturation buildup with interleaved FLASH readouts and radial k-space sampling for efficient, motion-resistant CEST imaging was employed. Each TR included a saturation pulse (100 ms, $B_{1,peak}$ = 2.4 µT), followed by a 7.5-degree flip angle pulse (TR/TE = 110 ms/1.22 ms) (Figure 1C). Fluorescence imaging was performed using an IVIS Spectrum CT with excitation at 554 nm and emission at 581 nm, with a 6-second exposure time and a 13 cm field of view.

Results: Figure 1A displays schematic of transgene construct for tdTomato (control) and superCESTide/tdTomato (CEST) viruses. Figure 1B shows fluorescence images indicating that fluorescence is predominantly localized in the liver for both rAAV-injected groups, with no fluorescence detected in the uninjected mouse, confirming successful viral transduction. The region of interest(ROIs) were defined over liver as shown in Figure 1 D,G and analyzed. The mouse injected with rAAV encoding superCESTide (Figure 1E,F) exhibited significantly higher CEST contrast compared to the control (Figure 1H,I) for both the Gaussian pulse and the PRECISE pulse respectively. As shown in Figure 1J, there is a significant correlation (R2 = 0.645, P value = 0.005) between the ratio of superCESTide to beta-actin, as determined by RT-PCR, and the CEST MRI contrast.

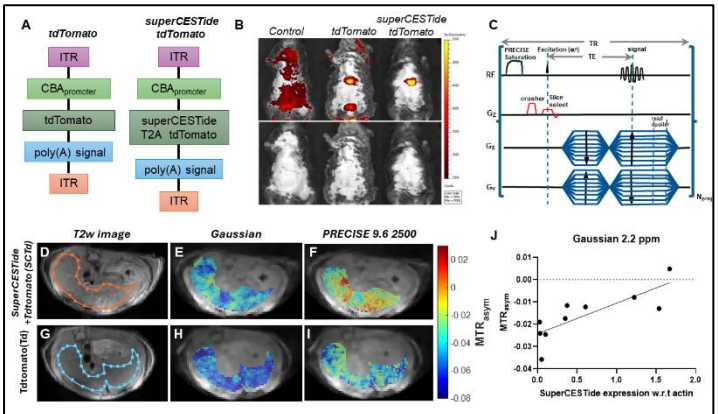

Figure 1 **A**. Schematic of transgene construct for tdTomato (control) and superCESTide/tdTomato (CEST) viruses; **B**. Fluorescence images of uninjected mouse, tdtomato and superCESTide+tdTomato mice; **C**. Steady state CEST sequence consisting of a saturation pulse, low flip angle excitation and gradient echo readout and radial k-space sampling; **D,G**. T2-weighted images; MTR_{asym} maps overlayed over respective CEST M_0 MR images at week 5 post-injection of tdtomato and superCESTide+tdTomato mice respectively using **E,H**. Gaussian and **F,I**. PRECISE 9.6 2500 pulse; **J.** Correlation of the ratio of superCESTide to beta-actin determined via RT-PCR

Conclusion: A strong correlation between CEST contrast and superCESTide expression was observed, highlighting the potential of using this MRI reporter gene for in vivo monitoring of gene expression.

References: i) Fillion, Adam J., et al. 2023. 11, NMR in Biomedicine, Vol. 36, p. e5007. ii) **Mohanta, Z.,et al. 2024** *bioRxiv*, pp.2024-06

Osmotic Blood-Brain Barrier Opening 2.0

Authors: Guanda Qiao[1], Chengyan Chu[1], David Gulisashvili[1], Shalini Sharma[1], Lukasz Kalkowski[1], Lucia Fadon-Padilla[1], Josh Ostovitz[1], Wojciech G. Lesniak[2], Daniel Deredge[3], Maciej Walczak[1,4], Lei Zhang[1], Anna Jablonska[1], Yajie Liang[1], Dheeraj Gandhi[1], Piotr Walczak[1], Miroslaw Janowski[1]

[1]Department of Diagnostic Radiology and Nuclear Medicine, School of Medicine, University of Maryland, Baltimore, MD 21201, USA. [2]Department of Radiology, Johns Hopkins School of Medicine, Baltimore, MD 21205, USA. [3]Department of Pharmaceutical Sciences, School of Pharmacy, University of Maryland, Baltimore, MD 21201, USA. [4]University of Maryland Baltimore County, Baltimore, MD 21250, USA

Background: The blood-brain barrier (BBB) poses a significant challenge in delivering therapeutic agents to the central nervous system (CNS) for treating neurological diseases. Osmotic blood-brain barrier opening (OBBBO) using an intra-arterial injection of 25% mannitol is a promising technique, but its efficacy and precision require further refinement.

Objective: This study aims to enhance the OBBBO efficacy by combining 25% mannitol with 4% NaCl to double osmotic power. We anticipate boosting the delivery of therapeutic agents, including biological drugs like antibodies, to the brain while keeping the procedure safe.

Methods: OBBBO was induced by intra-arterial delivery of a combination of 25% mannitol and 4% NaCl and compared with the current standard of intra-arterial 25% mannitol. It was immediately followed by systemic delivery of a model small molecule – Gadolinium-based contrast agent, or intra-arterial delivery of antibodies. BBB permeability to small molecules was assessed by MRI, and to biological drugs by radiolabeling of antibodies and subsequent PET imaging. Safety of the procedure was determined by follow-up MRI scans and *post-mortem* histology.

Results: We observed BBB opening after the intra-arterial administration of 25% mannitol, as anticipated. However, a combination of 25% mannitol with 4% NaCl radically boosted BBB opening territory and intensity by severalfold, both small molecules and biological drugs (Fig.1). As previously reported 25% mannitol is opening BBB mostly in the deep structures of posterior parts of the brain, while doubling osmotic power by addition of 4% NaCl to 25% mannitol effectively open BBB in the entire brain hemisphere. BBB opening in the anterior and middle parts of the brain is especially precious as this brain area is a target for the majority of therapeutic targets, such as brain cancer models. Follow-up MRI scans and histological analysis revealed no significant adverse effects on brain structure or function, with no evidence of tissue damage or inflammation. No significant differences in animal behavior or survival rates were observed between the treated and control groups, supporting the procedure's safety.

Conclusion: The combined use of 25% mannitol and 4% NaCl represents a significant improvement in OBBBO, offering a more effective method for delivering therapeutic agents to the brain. Moreover, the outstanding safety of procedures was confirmed by MRI scans and histological analysis. These findings support further optimization and large animal studies, paving the way for potential clinical translation. In summary, our new procedure resulted in extensive, consistent, and reproducible BBB opening across different brain regions

Funding: This work was supported by NIH R01NS120929 and R01DA056739. Based on these findings, a provisional patent application has been submitted.

Keywords: Blood-brain barrier, osmotic opening, mannitol, sodium chloride, therapeutic delivery, antibody radiolabeling, MRI, PET imaging.

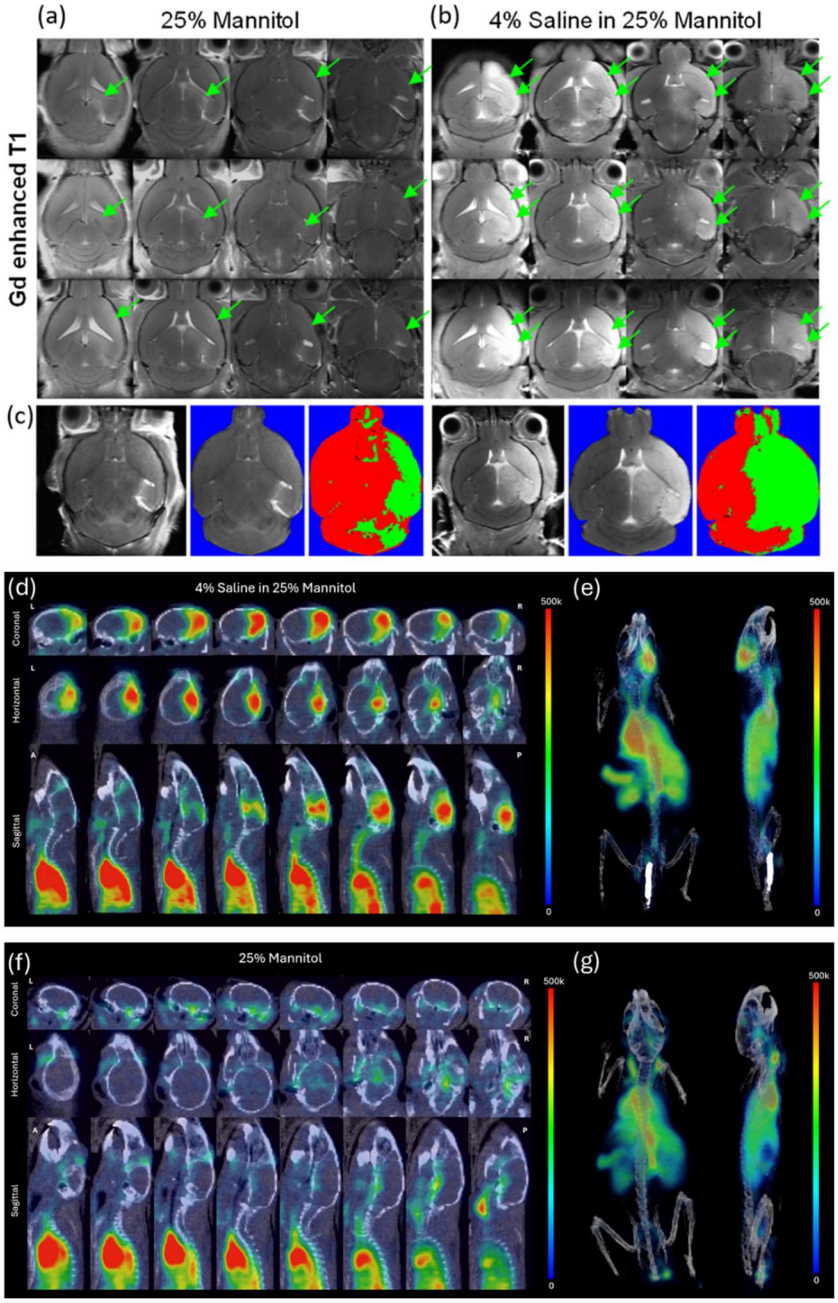

Figure 1. OBBBO territory of (**a**) Gd enhanced T1 MRI after 25% mannitol-induced BBBO (ImageJ lookup tables – Fire), horizontal view, green arrows represent areas of BBB opening. (**b**) Gd enhanced T1 MRI after BBBO with 4% saline in 25% mannitol (ImageJ lookup tables – Fire), horizontal view, green areas represent areas of BBB opening. (**c**) Segmentation of pixels below (red area) and above (green area) a set threshold identified using a custom Python script, representing an intact BBB and BBB opening, respectively. **PET/CT imaging after OBBBO**. (**d**) OBBBO using 4% saline in 25% mannitol followed by IA 89Zr-BVDFO injection. (**e**) Whole-body PET/CT 3D reconstruction after OBBBO with 4% saline in 25% mannitol followed by IA 89Zr-BVDFO injection. (**f**) OBBBO using 25% mannitol followed by IA 89Zr-BVDFO injection. (**g**) Whole-body PET/CT 3D reconstruction after OBBBO with 25% mannitol followed by IA 89Zr-BVDFO injection.

A Novel Genetically Encoded Reporter System for Functional Single-Cell Tracking in Cultured Mammalian Cells

Shylah Healy[1,2], Jinghui Wang[2], Miroslaw Janowski[2], Piotr Walczak[2], Yajie Liang[2]
[1]Johns Hopkins University, Baltimore, MD
[2]Department of Diagnostic Radiology and Nuclear Medicine, University of Maryland, Baltimore, Baltimore, MD

Background: Tumor heterogeneity, characterized by distinct changes between cells within the same tumor, is the main cause of drug resistance and relapse of cancers. The development of the genetically encoded fluorescent ubiquitination-based cell cycle indicator (FUCCI) system (**Fig. 1A**) [1] has expanded the toolset for investigating tumor heterogeneity, allowing for the visualization of the cell cycle phase in cancer cells. If a single cell's physical position, progression through the cell cycle, and activation of intracellular calcium signaling pathways can be tracked, then we can tell if there is any cellular heterogeneity present within a cancer cell population. However, the blue fluorescent protein (BFP), conventionally used in imaging, is not ideal for in vitro single-cell tracking because of the high background in culture medium. There are also no current sensors that can detect both calcium and the cell cycle, as calcium is an important second messenger for intracellular signaling pathways. Lastly, limited access to instruments capable of high throughput long-term imaging has prevented the exploration of this method.

Objective: We aim to explore whether a new genetically encoded reporter construct can reliably report migration, cell cycle progression, and calcium through long-term single-cell tracking.

Methods: We replaced the BFP in the FUCCI system with infrared fluorophore (miRFP670nano) and incorporated a calcium indicator (GCaMP6s [3]) to create the construct named functional FUCCI, illustrated in **Fig. 1B**. We then packaged lentivectors and transduced HEK293 cells and performed long-term single-cell tracking through repetitive imaging of these cells at 15 min intervals for 24 hours using Tecan Spark Cyto. These images from four channels (red, green, infrared, and bright field) were stacked and registered in ImageJ. In Cellpose [4], a customized segmentation model for HEK293 cells was then trained through manual annotation and applied to a cropped stack of the recorded images. Finally, Trackmate [5] was utilized to link the segmented cells together over consecutive time frames. A flowchart for this methodology is represented in **Fig. 1C**. The cell track labeled 'Track 1' was chosen for analysis of fluorescent intensity regarding both cell cycle indicator and GCaMP6s [5] calcium indicator.

Results: We successfully created a genetically encoded reporter system and tracked the dynamic change in the fluorescence intensity of functional FUCCI regarding cell cycle progression and calcium dynamics in HEK293 cells. We first analyzed the fluorescent intensity of the red channel and infrared channel (pseudo-colored as green) with respect to Track 1 over the recorded 96 time points, as shown in **Fig. 1D**. Expression of red and infrared fluorescence and their associated intensities are consistent with the cell's division and progression through the cell cycle, as confirmed by imaging of Track 1. **Fig. 1E** follows Track 1 over the same time frame and shows the fluorescent intensity of calcium. This analysis shows an increase in calcium intensity as this cell divides and provides insight into the dynamic calcium change within the cell. Successful application of Cellpose [4] and Trackmate [5] allowed for the segmentation and tracking of approximately 30 ROIs over the recorded time frame, as well as the illustration of each cell's migration track, as seen in **Fig. 1F**. The varying track lengths and displacements between cells shows that cellular heterogeneity can be seen using single-cell tracking.

Conclusions: We developed a genetically encoded reporter system that successfully tracks changes in fluorescence intensity of functional FUCCI, tracking cell cycle progression and calcium dynamics of single cells. Future studies should be performed to evaluate tumor heterogeneity and if similar behaviors can be observed in differing cell lines or in vivo. Moreover, the quantification of such behaviors may eventually allow for discovery of new drugs and potential treatment to combat cancer relapse.

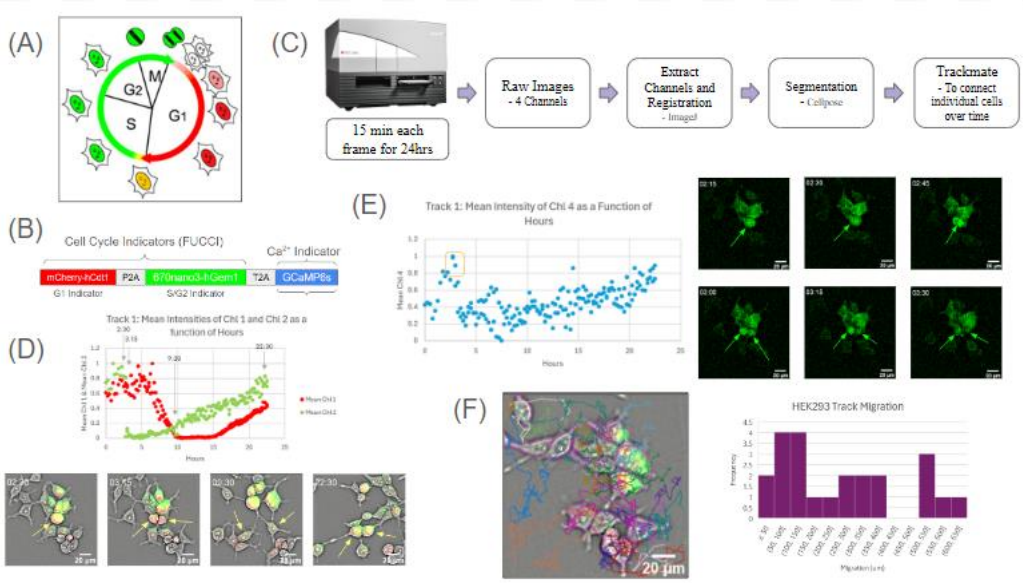

Figure 1: A. Schematic representation of FUCCI labeling G1 phase red and S/G2/M phases green [1]. **B.** Construct of functional FUCCI. **C.** Flowchart of HEK293 cell analysis. **D.** Mean intensities of cell cycle indicator in Track 1 with associated cell imaging. **E.** Mean intensity of calcium indicator in Track 1 with associated cell imaging. **F.** Cell imaging of single-cell tracking with illustrated migratory tracks and histogram of total migration per track.

References:

1. Sakaue-Sawano A, Kurokawa H, Morimura T, Hanyu A, Hama H, Osawa H, Kashiwagi S, Fukami K, Miyata T, Miyoshi H, Imamura T, Ogawa M, Masai H, Miyawaki A. Visualizing spatiotemporal dynamics of multicellular cell-cycle progression. Cell. 2008 Feb 8;132(3):487-98. doi: 10.1016/j.cell.2007.12.033. PMID: 18267078.

2. Liang Y, Walczak P. Long term intravital single cell tracking under multiphoton microscopy. J Neurosci Methods. 2021 Feb 1;349:109042. doi: 10.1016/j.jneumeth.2020.109042. Epub 2020 Dec 16. PMID: 33340557.

3. Chen, TW., Wardill, T., Sun, Y. *et al.* Ultrasensitive fluorescent proteins for imaging neuronal activity. *Nature* **499**, 295–300 (2013). https://doi.org/10.1038/nature12354

4. Stringer, C., Wang, T., Michaelos, M. *et al.* Cellpose: a generalist algorithm for cellular segmentation. *Nat Methods* **18**, 100–106 (2021). https://doi.org/10.1038/s41592-020-01018-x

5. Ershov, D., Phan, MS., Pylvänäinen, J.W. *et al.* TrackMate 7: integrating state-of-the-art segmentation algorithms into tracking pipelines. *Nat Methods* **19**, 829–832 (2022). https://doi.org/10.1038/s41592-022-01507-1

Combination of PD1 Immune Checkpoint Inhibition and the VEGF-A Growth Factor Scavenging Contributes to Restoring the Cytotoxicity of Exhausted T Cells against Glioblastoma *In Vitro*

Shriya Madan BSc[1], Anna Andrzejewska PhD[1], David Gulisashvili MD[1], Graeme Woodworth MD FACS [2], Debra Kukuruga PhD[3], Yajie Liang PhD[1], Piotr Walczak MD PhD[1], Miroslaw Janowski MD PhD[1]
[1]Department of Diagnostic Radiology, University of Maryland Baltimore, [2]Department of Neurosurgery, University of Maryland Baltimore, [3]Department of Pathology, University of Maryland Baltimore

Background: Glioblastoma (GBM), a highly aggressive brain cancer, remains elusive to all therapeutic strategies, including the Nobel Prize-winning immune checkpoint inhibitors (ICIs). It is also characterized by intratumoral T cell exhaustion and extremely high local concentrations of vascular endothelial growth factor A (VEGF-A).

Objective: We hypothesize that (VEGF-A) aggravates local immunosuppression, preventing the induction of T cell cytotoxicity by ICIs. Therefore, we studied *in vitro* the impact of ICIs and VEGF-A scavenging in monotherapy or combinations on cytotoxicity against GBM of T cells at various states (activated, primed, and bead- or cell-exhausted).

Methods: ELISA was used to determine VEGF-A production by luc(+) GBM and subsequent scavenging efficacy of anti-VEGF-A antibody (bevacizumab) *in vitro*. HLA-matched T cells were activated using anti-CD3/CD28 beads, then primed through transient exposure to GBM and exhausted using repetitive exposure to anti-CD3/CD28 beads or by culturing them with GBM cells. Co-cultures of these T cells at each of the four states with GBM at a 1:1 ratio was used to study the effect of 3 concentrations of nivolumab, ipilimumab, anti-PDL1 antibody, and bevacizumab over five days. Normalized bioluminescence served as a dependent variable to report on GBM cell death. Independent variables included 1) antibodies, 2) concentrations, 3) T cell status, and 4) observation period. All experiments were performed with three biological and three technical replicates. The dataset was subjected to multivariate, hierarchical regression using fixed and random effects (PROC MIXED, SAS 9.4).

Results: VEGF-A ELISA results showed significant production of VEGF-A by GBM and that the addition of bevacizumab to the GBM cells nearly completely scavenged VEGF-A from culture media. We have also demonstrated the therapeutic effect of a combination of anti-PD1 ICI and VEGF-A scavenging in co-cultures of GBM-exhausted T cells, which was statistically significant.

Conclusions: Combining PD-1 ICI and VEGF-A scavenging can be considered a potential treatment for GBM as it partially restores the cytotoxicity of exhausted T cells. However, to reproduce these results in vivo, excellent penetration of antibodies across the blood-brain barrier might be required.

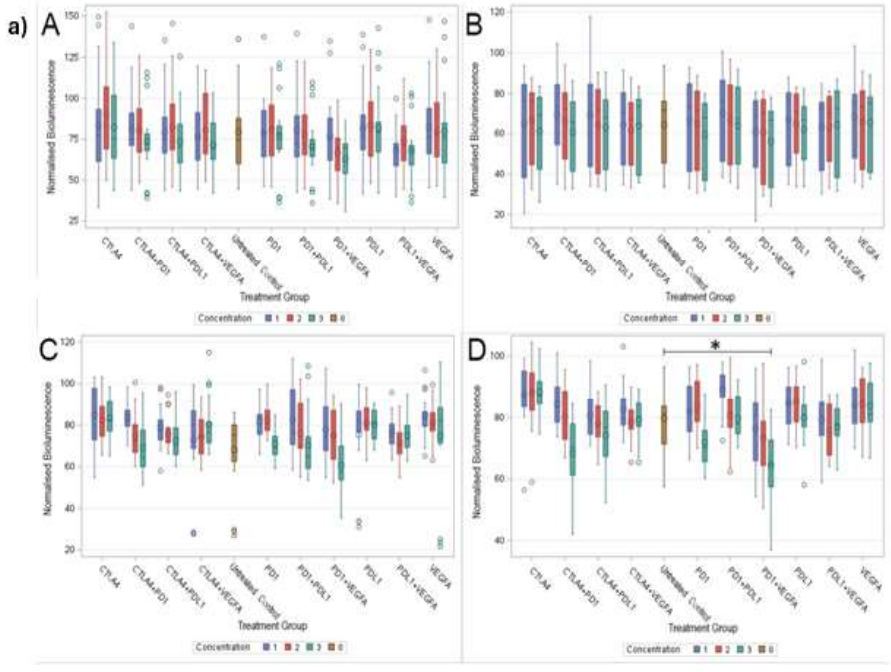

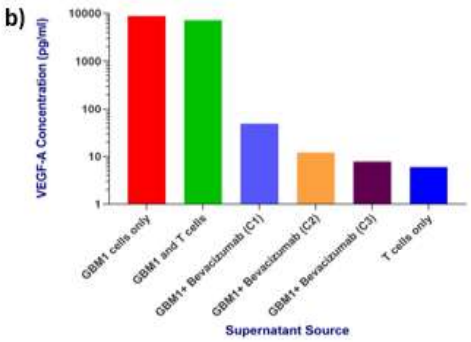

Figure : a) *In vitro* therapeutic efficacy of T cells at various stages (A- activation, B - priming, C - anti-CD3/CD28 bead-induced exhaustion, D - GBM cell-induced exhaustion) against GBM1 cells. A combination of VEGF-A and PD-1 blockade is the most effective in co-culture GBM1-luc with cell-exhausted T cells (*p value <0.05) b) VEGF-A measured by ELISA in supernatants of GBM cells with or without treatment of Bevacizumab. NOTE: y-axis shows a logarithmic scale.

Intraperitoneal Ovarian Cancer Imaging Enhanced by BrCy112: Dual-Mode-Dual-Gd Contrast Agents in Near-Infrared Imaging

Bonghwan Chon, PhD[1], Mukesh P. Yadav, PhD[1], William Ghann, PhD [2], Jamal Uddin, PhD [2], Bahman Anvari, PhD[3] and Vikas Kundra, MD, PhD [1,4*]

[11]Department of Diagnostic Radiology and Nuclear Medicine, University of Maryland School of Medicine, Baltimore, MD, USA [2] Center for Nanotechnology, Coppin State University, Baltimore, MD, USA [3] Department of Bioengineering and Department of Biochemistry, University of California, Riverside, CA, USA [4]Marlene and Stewart Greenebaum NCI Comprehensive Cancer Center Program in Oncology, Experimental Therapeutics, University of Maryland School of Medicine, Baltimore, MD, USA

Background: Ovarian cancer, the deadliest gynecologic malignancy, often presents at an advanced stage within the peritoneal cavity, leading to poor survival rates. Accurate tumor localization and characterization are crucial for staging and pre-surgical planning, but current clinical methods like CT or MR with traditional contrast agents have limited sensitivity and only temporary tumor enhancement. The extent of tumor resection significantly impacts survival, yet detecting tumors within the peritoneal cavity is challenging. A multimodal imaging agent combining MR for pre-surgical planning and optical imaging for surgical removal could transform ovarian cancer imaging. The only clinically approved near infrared (NIR) agent, ICG, has limited quantum yield and readily aggregates in aqueous solution, limiting its optical properties. There remains potential to improve optical properties such as stability and fluorescence quantum yield by controlling donor and acceptor components. The introduction of heavy bromine atoms increases the fluorescence quantum yield and stability of heptamethine cyanine dyes. This study aims to evaluate a dual-mode, dual-gadolinium (DMDG) liposomal contrast agent for visualizing intraperitoneal ovarian tumors using multimodal MR and NIR imaging, potentially offering greater relaxivity, fluorescence prolonged tumor retention, and improved imaging capabilities.

Objective: To evaluate imaging capability of NIR fluorophore BrCy112 in dual mode dual Gd (DMDG) nanoparticle formulation for MR and NIR imaging of intraperitoneal ovarian cancer.

Methods: We utilized dual-mode, dual-Gadolinium (DMDG) nanoparticles equipped with either of two different NIR fluorophores (ICG and BrCy112) along with magnetic resonance (MR) imaging agents. The optical properties of the NIR fluorophores were evaluated in vitro using absorption and fluorescence spectroscopy. For liposomal formulation, the loading concentrations of the NIR fluorophores were optimized for DMDG-ICG and DMDG-BrCy112, respectively. In vitro characterization of these nanoparticles included assessments of particle size and their magnetic/optical properties for dual imaging purposes. Subsequently, we conducted MR and NIR fluorescence imaging studies in intraperitoneal ovarian cancer models.

Results: In DI water, the fluorescence intensity of BrCy112 was ~2.5 times greater than that of ICG ($p<0.05$, n=5). In liposomal formulations with optimized loading concentrations, DMDG-BrCy112 exhibited FL intensity in the NIR region of ~three times greater than DMDG-ICG ($p<0.05$, n=5). Intraperitoneal ovarian tumors (HeyA8) in mice showed enhanced MR signals two days after intravenous injection of either DMDG-BrCy112 or DMDG-ICG compared to controls. Open abdomen and excised tumor analysis revealed animals injected with DMDG-BrCy112 had twice the FL intensity (radiant efficiency)/g tumor compared to those injected with DMDG-ICG ($p < 0.05$, n = 6).

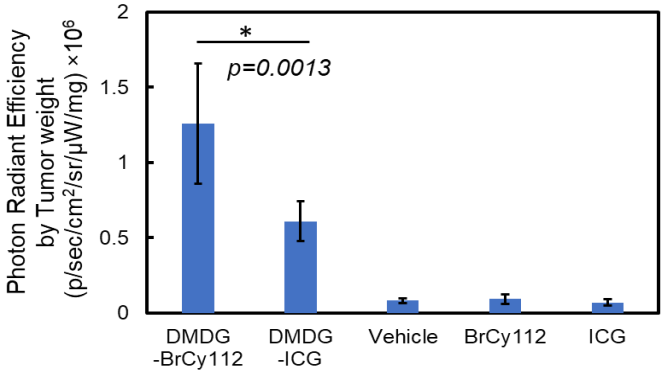

Figure. Semi-quantitative evaluation of fluorescence after two days of injected imaging agents: DMDG-BrCy112, DMDG-ICG, vehicle, free-BrCy112, and free-ICG. ($P < 0.05$, n=6).

Conclusions: BrCy112 has greater fluorescence than ICG and in nanoparticle (DMDG) can be used days after a single injection for MR and NIR imaging of intraperitoneal ovarian tumors in a mouse model suggesting clinical potential for pre-surgical planning and image-guided resection of intraperitoneal ovarian cancer.

A Low Power Bluetooth Microscope for Multicontrast Function Imaging

Subhrajit Das[1], Janaka Senarathna[2], Yunke Ren[3], Irfan Karim[4], Ralph Etienne-Cummings[1] and Arvind P. Pathak[1,2,3]
Dept. of [1]Electrical and Computer Engineering, [2] Radiology and Radiological Science, and [3]Biomedical Engineering, Neurology[4], Johns Hopkins University, Baltimore, MD 21218.

Introduction: Innovative miniaturized microscopes, or "miniscopes," are crucial for understanding the link between neurovascular changes and behavior in animals. Despite their advanced capabilities, a significant drawback is their reliance on tethers or wires for power, data transfer and control. These tethers restrict natural animal behavior and complicate experiments with multiple animals due to the potential for entanglement. Therefore, developing wireless miniscopes is essential. Creating a wireless miniscope necessitates a small, onboard battery, which poses a challenge because even lightweight batteries can burden a small rodent. One promising direction is utilizing low-power surveillance systems, such as the RSL10 smart shot camera evaluation board. This board integrates a Bluetooth Low Energy (BLE) 5.2 System-on-Chip (SoC) and a low-power CMOS image sensor. By adapting this board with an optical front end, we developed the “BLEscope”. The BLEscope streams images from a rodent’s sensory motor cortex at 1 frame per second (fps) over BLE to a smartphone or laptop. Here we demonstrated BLEscope’s versatility for functional imaging applications via in vivo experiments in anesthetized animals (due to the size of this proof-of-concept system). BLEscope paves the way for the future development of completely miniaturized, wireless microscopes, enhancing the study of natural animal behavior and their correlative neurovascular dynamics.

Materials and Methods: The BLEscope leverages an RSL10 smart shot camera evaluation board integrated with a custom 3D-printed microscope as shown in **Fig. 1a**. This setup utilizes a long-pass filter with a 510 nm cutoff to block blue excitation light. An aspheric lens with a focal length of 4.6 mm focuses images onto a CMOS sensor (ARX3A0). The entire assembly is powered by a 3.7 V LiPo battery. Control of the BLEscope is possible through a smartphone app, PC or laptop, offering two modes: "streaming" for continuous video and "single image capture." The wireless control process is illustrated in **Fig. 1b**. Here, a laptop locates the BLEscope, and connects via a MATLAB® script. The BLEscope's operation is managed using specific opcodes. For "single image capture," the laptop sends opcode 0x01, triggering image acquisition. The BLEscope then notifies the laptop of the image size, after which the laptop requests the data using opcode 0x04. For "streaming" mode, opcode 0x02 is sent to start the continuous image capture, and the laptop continually sends opcode 0x04 with 1s pauses to ensure complete data transfer. The mode is terminated with opcode 0x03. To test the BLEscope's in-vivo imaging capabilities, a carbogen inhalation experiment was performed on two mice with brain tumors. Animals were anesthetized with 1.5% isoflurane and secured on the imaging platform; images were captured at 1 fps in "streaming" mode. A five-minute baseline was recorded with room air, followed by carbogen gas for another five minutes, and a 15-minute period of room air inhalation.

Results, Discussion and Conclusion: Using the FL channel of the BLEscope, we successfully monitored GFP-expressing brain tumor cells in vivo, as illustrated in **Fig. 1c** and **1f**. The same field of view (FOV) was captured using the IOS channel, and the mean IOS maps over 25 minutes for each animal are shown in **Fig. 1d** and **1g**. To evaluate hemodynamic changes induced by carbogen in tumor-associated and normal blood vessels, we selected four regions of interest (ROIs) shown in **Fig. 1d** and **1g**. These ROIs included the tumor region, a non-tumor background region, a tumor-associated blood vessel, and a normal blood vessel distant from the tumor. The IOS time-series for these ROIs are plotted in **Fig. 1e** and **1h**, respectively. Our analysis of the time-series data (**Fig. 1e** and **1h**) revealed that the tumor region and the tumor-associated blood vessel exhibited a diminished hemodynamic response to carbogen inhalation compared to the non-tumor background region and the normal blood vessel. This suggests that the presence of the tumor alters the local hemodynamic response, reducing sensitivity to vasodilatory stimuli like carbogen. Additionally, the BLEscope consumed an average current of ~66 mA in "streaming" mode, allowing for ~1.5 hours of continuous imaging at 1 fps with a 100 mAh battery. A miniaturized version of BLEscope could significantly contribute to our understanding of brain function.

Acknowledgements: This work was supported by NIH grant nos. 2R01CA196701, 5R01CA237597-04, and 5R01DE027957-05.

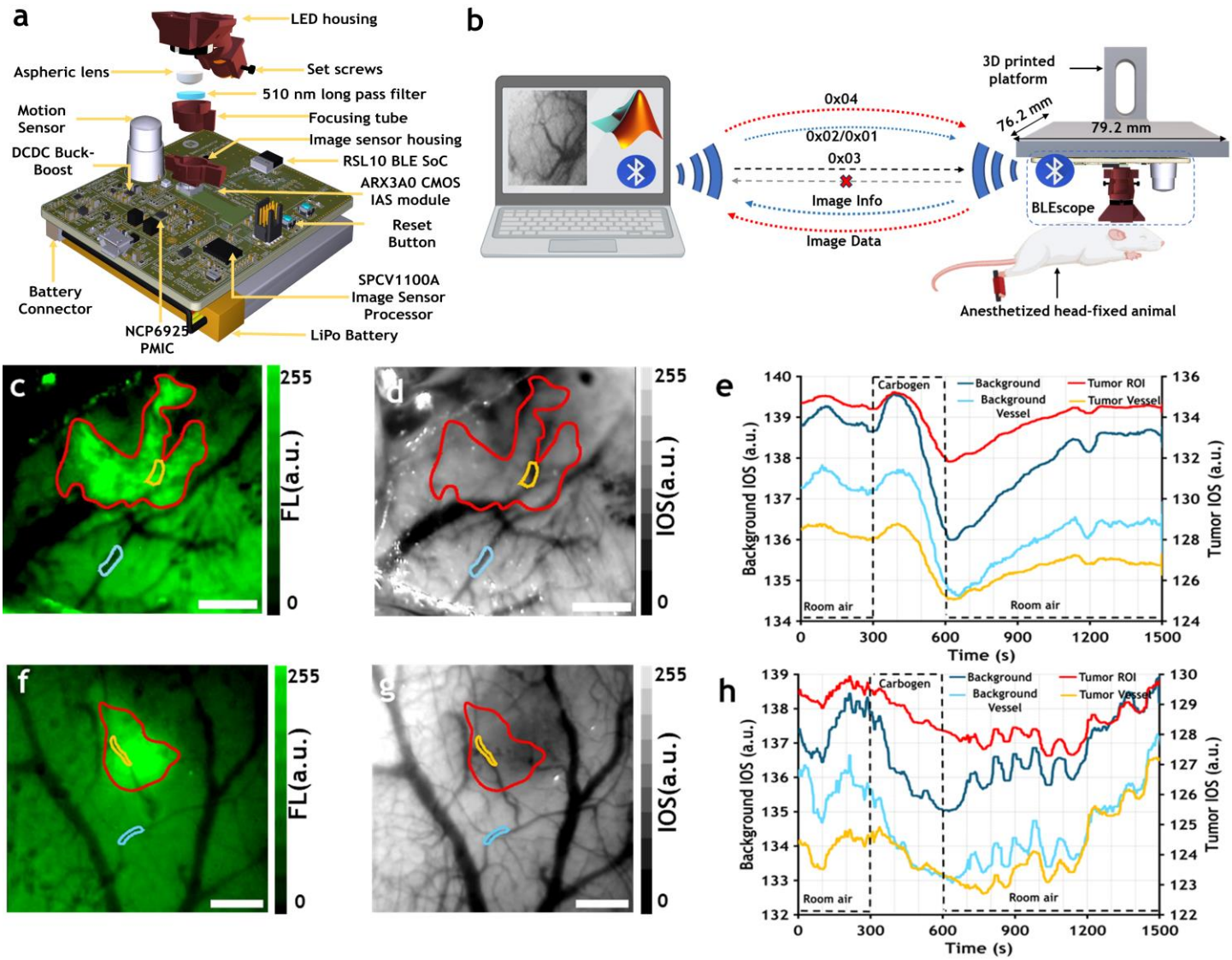

Fig. 1: A Low Power Bluetooth Microscope for Multicontrast Function Imaging. (a) The 'BLEscope' is shown in an exploded view, displaying its various components: the dual LED housing, an aspheric lens, and a focusing tube. The setup also includes a 100 mAh 3.7 V LiPo battery. Key elements on this board include the RSL10 BLE SoC, the CMOS ARX3A0 image sensor, the SPCV1100A Image Sensor Processor (ISP), and the NCP6925 Power Management IC (PMIC), all arranged in relation to the microscope. **(b)** The wireless control flow and experimental setup for in vivo neuroimaging using the BLEscope are depicted. The experiment utilized a 3D-printed platform to hold the evaluation board securely, focusing on the animal's somatosensory cortex. Wireless communication was established between a laptop and the BLEscope via opcodes 0x01 or 0x02, represented by a blue dotted arrow from the laptop to the BLEscope. The BLEscope captured an image and sent the image information back to the laptop, shown by another blue dotted arrow. The laptop requested image data using opcode 0x04, illustrated by a red dotted arrow, and the BLEscope receiving the data, indicated by another red dotted arrow. To end the transmission, opcode 0x03 was sent from the laptop, with a red cross on the black dotted arrow indicating the termination. **(c)** and **(f)** display the mean fluorescence images of GFP-expressing brain tumor cells from the two mice. The animals breathe room air for 300 seconds, followed by carbogen gas (95% O2 and 5% CO2) for another 300 seconds, and then room air again for 900 seconds. Specific regions of interest (ROIs) were selected to map hemodynamic changes using the intrinsic optical signal (IOS) channel. **(d)** and **(g)** present mean IOS maps corresponding to the same field of view as in **(c)** and **(f)**. **(e)** and **(h)** illustrate IOS time-series data, representing hemodynamic changes in the background or tumor ROIs during carbogen inhalation, with the changes shown on the secondary y-axis and the dashed lines marking the inhalation periods.

Enhancing Treatment of Diffuse Intrinsic Pontine Glioma: Synergistic Effect of Focused Ultrasound and Anti-CD47 Immunotherapy

D. Gulisashvili[1], P. Anastasiadis[2], G. Qiao[1], A. Jablonska[1], S. Madan[1], A. Andrzejewska[1], S. Sharma[1], L. Kalkowski[1], M. Migliorini[2], D. Strickland[2], D. Deredge[3], Y. Liang[1], C. Civin[4], P. Walczak[1], G. Woodworth[5], M. Janowski[1]

[1]Department of Diagnostic Radiology and Nuclear Medicine, School of Medicine, University of Maryland Baltimore, MD 21201, USA.
[2]Center for Vascular and Inflammatory Diseases and the Departments of Surgery and Physiology, University of Maryland School of Medicine, Baltimore, Maryland 21201.
[3]Department of Pharmaceutical Sciences, School of Pharmacy, University of Maryland, Baltimore, MD 21201, USA
[4]Departments of Pediatrics and Physiology, School of Medicine, Center for Stem Cell Biology and Regenerative Medicine, University of Maryland, Baltimore, MD, 21201, USA.
[5]Department of Neurosurgery, School of Medicine, University of Maryland Baltimore, MD 21201, USA.

Background and Objective: Diffuse Intrinsic Pontine Glioma (DIPG), a fatal pediatric brain cancer with few treatment options,[1] faces drug delivery challenges due to the blood-brain barrier (BBB).[2] Focused ultrasound (FUS) is a novel method to open the BBB, improving therapeutic agent penetration.[3] Anti-CD47 (aCD47) immunotherapy has shown promising results in various solid cancers by promoting phagocytosis of cancer cells by the immune system.[4] This study investigates combining FUS BBB opening with systemic aCD47 administration to improve DIPG treatment efficacy.

Methods: The aCD47 antibody was conjugated to deferoxamine (DFO), and subsequently radiolabeled with zirconium-89 (89Zr) for imaging purposes. We utilized instant thin-layer chromatography (iTLC), high-performance liquid chromatography (HPLC) combined with a radioflowmonitor, mass spectrometry, and surface plasmon resonance (SPR) to validate the conjugation, radiochemical purity, and binding affinity of our construct. In vitro studies were conducted using luciferase-positive DIPG cells co-cultured with mouse bone marrow-derived macrophages to assess the therapeutic impact of CD47 blockade. In vivo, a DIPG mouse model was created using a previously established method,[5] with groups assigned to various treatments: IV aCD47 antibody, FUS alone, and a combination of FUS and IV aCD47 antibody, with the initial two animals treated in this group. 89Zr-aCD47 delivery to the brain was assessed with positron-emission tomography (PET) and a biodistribution study. Outcome measures included bioluminescence imaging (BLI), magnetic resonance imaging (MRI), and overall animal survival.

Results: Mass spectrometry revealed the binding of up to four DFO molecules per antibody (**Fig. 1A**), and SPR confirmed unaffected affinity to CD47 (**Fig. 1B**). ITLC revealed 97.4% radiochemical purity and HPLC-radioflowmonitor showed specific binding of 89Zr to the antibody (**Fig. 1C**). The mice treated with IV aCD47 antibody alone showed no response to treatment, and no change in survival was observed (**Fig. 1D**). Similarly, the mice treated with FUS alone showed no response to treatment (**Fig. 1E**). *In vitro*, CD47 blockade activated macrophages, reducing bioluminescence of DIPG cells (**Fig. 1F**). FUS resulted in the accumulation of aCD47 in the brain as detected by PET (**Fig. 1G**), which led to tumor eradication as detected by BLI (**Fig. 1H**) and MRI (**Fig. 1I**) without relapse for the subsequent three months.

Conclusions: Our findings provide evidence that combining FUS-mediated BBB opening with systemic administration of aCD47 antibody holds potential as a therapeutic strategy for DIPG. PET imaging served as a tool to validate the delivery of the antibody to the brain, underscoring the synergy between FUS and immunotherapy. Studies with larger sample sizes are warranted to further validate these promising results and explore the full therapeutic potential of this approach.

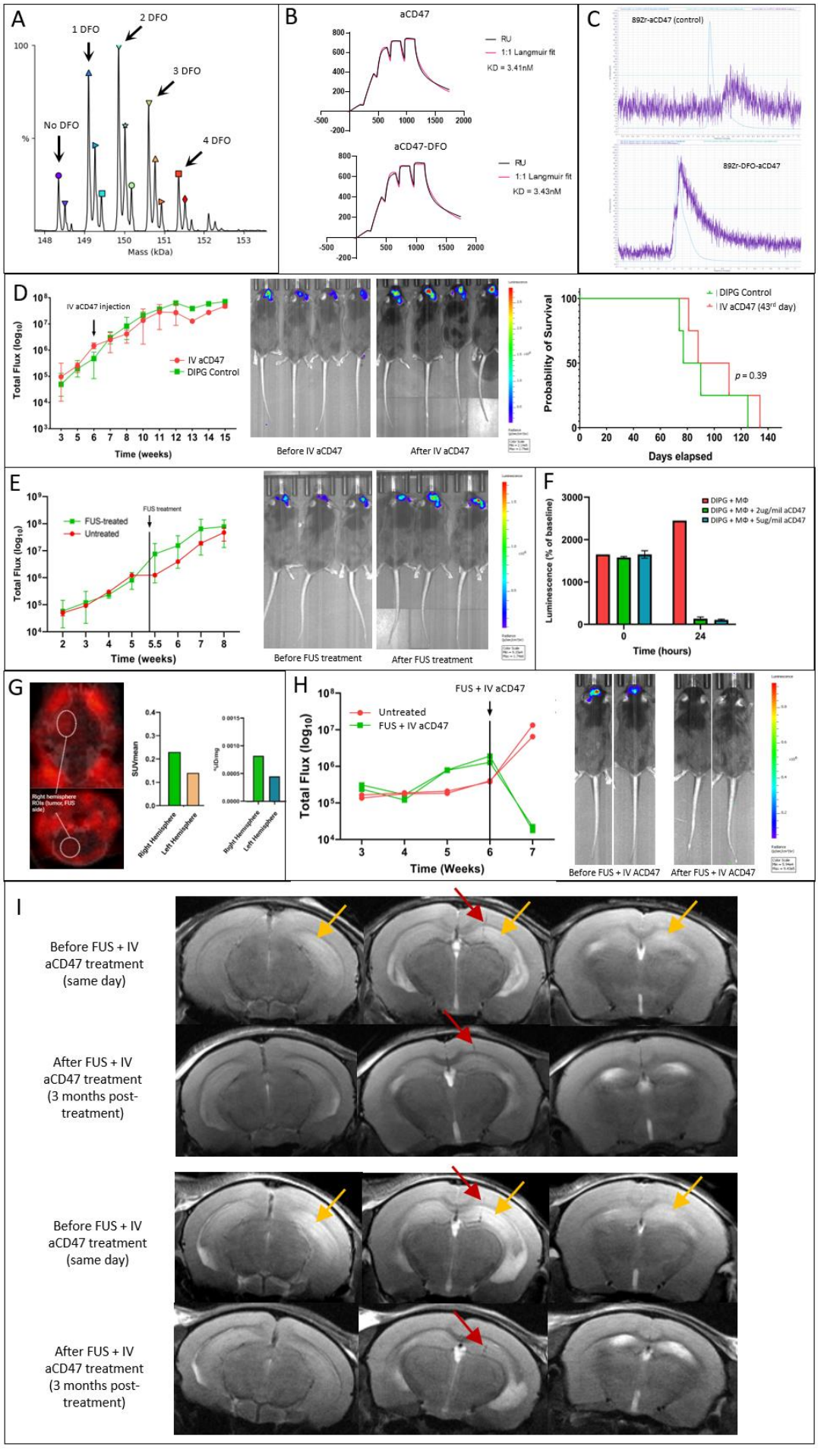
A
1 DFO
2 DFO
3 DFO
4 DFO
No DFO
100
%
148
149
150
151
152
153
Mass (kDa)
B
aCD47
RU
1:1 Langmuir fit
KD = 3.41nM
aCD47-DFO
RU
1:1 Langmuir fit
KD = 3.43nM
C
89Zr-aCD47 (control)
89Zr-DFO-aCD47
D
IV aCD47 injection
Total Flux (log10)
IV aCD47
DIPG Control
Time (weeks)
Before IV aCD47
After IV aCD47
DIPG Control
IV aCD47 (43rd day)
Probability of Survival
p = 0.39
Days elapsed
E
FUS-treated
Untreated
FUS treatment
Total Flux (log10)
Time (weeks)
Before FUS treatment
After FUS treatment
F
DIPG + MΦ
DIPG + MΦ + 2ug/mil aCD47
DIPG + MΦ + 5ug/mil aCD47
Luminescence (% of baseline)
Time (hours)
G
Right hemisphere ROIs (tumor, FUS side)
SUVmean
%ID/mg
Right Hemisphere
Left Hemisphere
H
FUS + IV aCD47
Untreated
FUS + IV aCD47
Total Flux (log10)
Time (Weeks)
Before FUS + IV ACD47
After FUS + IV ACD47
I
Before FUS + IV aCD47 treatment (same day)
After FUS + IV aCD47 treatment (3 months post-treatment)
Before FUS + IV aCD47 treatment (same day)
After FUS + IV aCD47 treatment (3 months post-treatment)

Figure 1. A. Mass spectrometry reveals up to 4 DFO attachments on aCD47. **B.** SPR shows unchanged binding of aCD47 to CD47 after DFO attachment. **C.** HPLC-radioflowmonitor confirms 89Zr chelation by aCD47-DFO. **D.** BLI timeline and images for mice treated with only IV aCD47 and their survival compared to untreated DIPG controls. **E.** BLI timeline and images for only FUS-treated mice and untreated DIPG controls. **F**. In vitro DIPG-macrophage co-culture with/without aCD47 **G.** PET images with SUV and biodistribution show an increased accumulation of radiolabeled aCD47 in the right hemisphere. **H.** BLI timeline and images for FUS + IV aCD47, achieving DIPG tumor eradication. **I**. MRI imaging of DIPG mice brain before and 3 months after treatment with FUS + IV aCD47 showing needle tracks from implantation (red arrows) with adjacent T2 hyperintensities (yellow arrows), which disappear after FUS + IV aCD47 treatment, suggesting tumor eradication.

References

1. Miguel Llordes G, Medina Pérez VM, Curto Simón B, Castells-Yus I, Vázquez Sufuentes S, Schuhmacher AJ. Epidemiology, Diagnostic Strategies, and Therapeutic Advances in Diffuse Midline Glioma. J Clin Med. 2023;12(16):5261. Published 2023 Aug 12. doi:10.3390/jcm12165261

2. Pardridge WM. Drug transport across the blood-brain barrier. J Cereb Blood Flow Metab. 2012;32(11):1959-1972. doi:10.1038/jcbfm.2012.126

3. Martinez P, Nault G, Steiner J, et al. MRI-guided focused ultrasound blood-brain barrier opening increases drug delivery and efficacy in a diffuse midline glioma mouse model. Neurooncol Adv. 2023;5(1):vdad111. Published 2023 Sep 12. doi:10.1093/noajnl/vdad111

4. Son J, Hsieh RC, Lin HY, et al. Inhibition of the CD47-SIRPα axis for cancer therapy: A systematic review and meta-analysis of emerging clinical data. Front Immunol. 2022;13:1027235. Published 2022 Nov 11. doi:10.3389/fimmu.2022.1027235

5. Lan X, Kedziorek DA, Chu C, et al. Modeling human pediatric and adult gliomas in immunocompetent mice through costimulatory blockade. Oncoimmunology. 2020;9(1):1776577. Published 2020 Jun 5. doi:10.1080/2162402X.2020.1776577

An Image-Informed Computational Model of Murine Cerebral Hemodynamics

Rebeca Hannah de M. Oliveira[1], M.S, Janaka Senarathna[2], PhD, Vu Dinh[2], M.S., Aleksander S. Popel[1],PhD, Arvind P. Pathak[2], PhD

1 Biomedical Engineering Department, The Johns Hopkins University School of Medicine, Baltimore, MD, USA

2 Russell H. Morgan Department of Radiology and Radiological Science, The Johns Hopkins University School of Medicine, Baltimore, MD, USA

Background: Models of cerebral blood flow (CBF) have been developed to advance our knowledge about the control mechanisms and the effect of pathological conditions on brain hemodynamics. Technological advancements in in vivo imaging allow us to more accurately account for structural and functional features of the cerebral vasculature and validate hemodynamic model predictions.

Objective: As a next step for advancing the modeling of cerebral hemodynamics, we present a novel approach in which the *in vivo* measurements of blood vessel diameter changes and the vascular network architecture are used to inform the CBF model and predict temporal hemodynamic changes in the murine brain.

Methods: From image data previously obtained from a healthy mouse brain in vivo using a multicontrast miniaturized microscope or "miniscope" developed by our group[1], we extracted changes in blood vessel diameters for multiple vascular segments within a 3 mm by 3 mm field-of-view (FOV). These diameter measurements were obtained every 5s for up to 10 min. We adapted a prior version of a hemodynamics model, which used geometrical vascular features (node connections, vascular coordinates, vessel length, and diameter) as inputs to incorporate temporal diameter measurements[2]. The brain region's hemodynamic characteristics were simulated based on the 1D formulation of Poiseuille's law and the hematocrit-dependent viscosity law. Using MATLAB®, we iteratively solved a system of algebraic equations that satisfied mass conservation within vessel nodes to derive nodal pressure and hematocrit distributions. Pressure and hematocrit values for each vascular segment were iterated until the system converged. The base model has been previously derived from experimental data by Pries et al[3]. To assign boundary conditions and identify arteriolar and venular nodes, we used FITC-labeled Dextran data to obtain the time-to-peak maps using the fluorescence channel of the miniscope. The pressure at venular nodes was set to 15 mmHg and the pressure of arteriolar boundary nodes was set using a Gaussian distribution ranked by vessel diameter to with mean at 75 mmHg and standard deviation of 10 mmHg. We predicted hemodynamic changes over time by updating the segment diameter with the in vivo data.

Results: Using a miniscope with a resolution of 6 μm, we measured the diameter for multiple blood vessel segments within the range of 6-120 μm. Using the Amira® software package for blood vessel segmentation, we found that the cerebrovascular network withing the FOV contained 553 segments, (Fig. 1a). Based on in vivo fluorescence data, we identified 28 arteriolar boundary nodes (inlets) and 15 venular boundary nodes (outlets) (Fig.1b). With our hemodynamic model, we simulated CBF variations caused by in vivo diameter changes obtained over 10 min for each vascular segment. The simulated CBF velocity during this period was 8.1 ± 9.95 mm/s. Fig.1c shows the evolution of blood flow from 5s to 10 minutes of simulation. We also predicted velocity, pressure, viscosity, hematocrit, and shear distributions (Figs. 1d-h). Overall, we obtained values within physiological ranges for the murine brain[2].

Conclusions: Our proposed modeling strategy enabled us to predict discrete time-dependent hemodynamic behavior within microvascular networks (i.e. arterioles and venules) of the mouse brain using in vivo image data, leading to results within reasonable physiological ranges. Our model can be applied to investigate region-dependent and time-dependent hemodynamic variations caused by pathological conditions such as stroke, seizures or tumors. Future approaches will include optimizing pressure at inlets to limit or eliminate segments with non-physiological CBF velocities, validation of velocity predictions and simulation of CBF changes in brain tumor-bearing mice. In summary, our modeling strategy provides a new platform to investigate temporal alterations in cerebral hemodynamics, enabling more physiologically relevant changes in brain function.

This work was supported by NIH grant nos. 2R01CA196701-06A1, 5R01CA237597-04 and 5R01DE027957-05.

References:

1. Senarathna, J. *et al.* A miniature multi-contrast microscope for functional imaging in freely behaving animals. *Nat. Commun.* **10**, 99 (2019).
2. Bhargava, A. *et al.* VascuViz: a multimodality and multiscale imaging and visualization pipeline for vascular systems biology. *Nat. Methods* **19**, 242–254 (2022).
3. Pries, A. R., Neuhaus, D. & Gaehtgens, P. Blood viscosity in tube flow: dependence on diameter and hematocrit. *Am. J. Physiol.* **263**, H1770-1778 (1992).

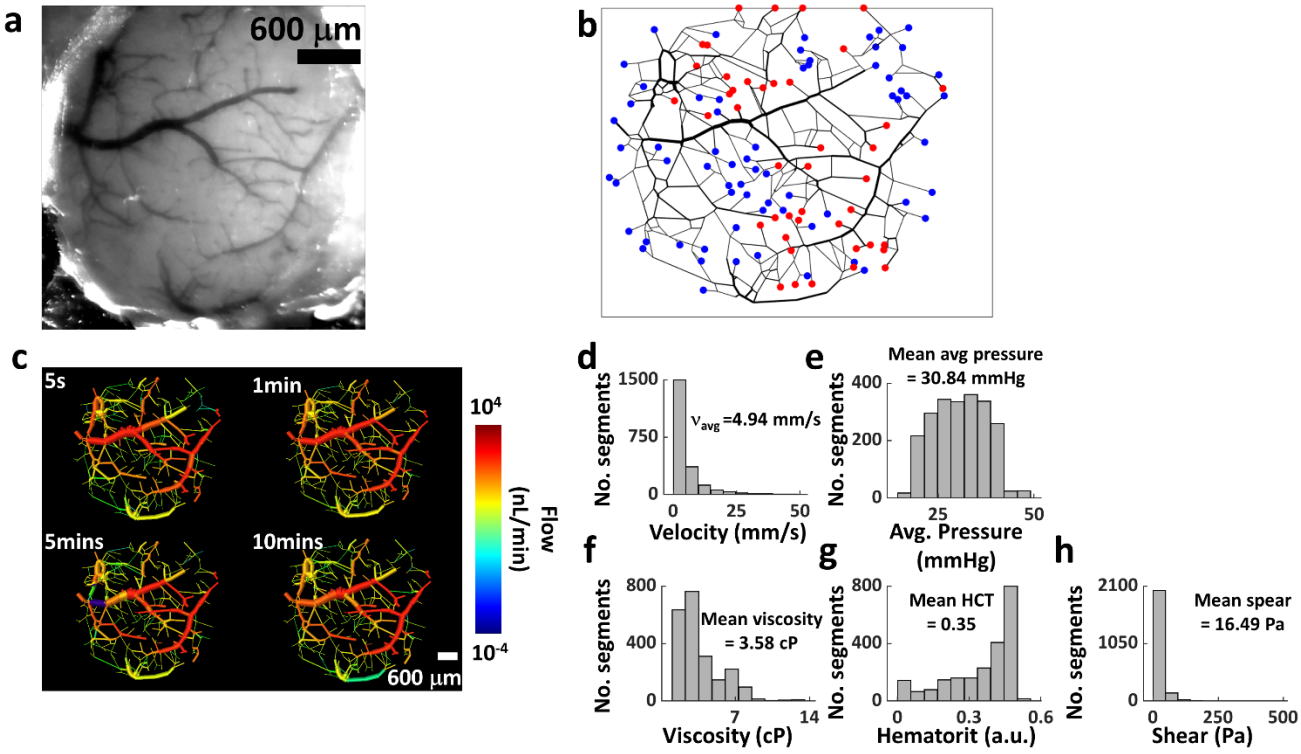

Figure 1: Discrete time-dependent variations in cerebral hemodynamics using an image-informed model.

Assessing Lactate Release in an Epilepsy Mouse Model using Metabolic Imaging of Hyperpolarized [1-^{13}C]Pyruvate

Aditya Jhajharia[1], Mitchell Moyer[2], Jemima Olu-Owotade[2], Abubakr Eldirdiri[1], Muznabanu Bachani[2], Joshua Rogers[1], Minjie Zhu[1] Alexander Ksendzovsky[2], Dirk Mayer[1]

[1]Department of Diagnostic Radiology and Nuclear Medicine, University of Maryland, Baltimore, MD, USA.
[2]Department of Neurosurgery, University of Maryland School of Medicine, Baltimore, MD, USA.

Background: Approximately 30% of epilepsy patients continue to experience seizures despite medical therapy. Outcomes in epilepsy surgery are dependent largely on correctly identifying, mapping, and subsequently treating the epileptogenic focus (EF) or seizure onset zone (SOZ). High glucose metabolism, lactate dehydrogenase A (LDHA), and elevated lactate (Lac) production are linked to epilepsy (1,2), suggesting Lac as a potential non-invasive biomarker for localizing epileptic tissue.

Objective: This study aims to apply dynamic magnetic resonance spectroscopic imaging (MRSI) of hyperpolarized (HP) [1-^{13}C]Pyruvate (Pyr) to accurately measure Lac elevations in a Pentylenetetrazol (PTZ) mouse model of epilepsy.

Methods: To model chronic epilepsy, kindling was induced in mice (n=9) through administration of sub-convulsive doses of PTZ (35 mg/kg, intraperitoneal), while control (sham) animals (n=8) received the PTZ vehicle, PBS, for 20 days on alternate days. Seizure responses in these treated mice were assessed using Racine behavioral scores. Forty-eight hours after final dose of PBS or PTZ, HP imaging was conducted using a pre-clinical 3 Tesla Bruker Biospec MR scanner (Bruker, Ettlingen, Germany). A fast dynamic spiral chemical shift imaging (spCSI) (3) scan with a multiband spectral-spatial RF pulse (4) was performed, allowing for the different excitation flip angles for substrate and product resonances. Following imaging, all mice were euthanized, and their brains were harvested to measure extracellular lactate concentrations using a fluorometric lactate assay kit (Cell Biolabs, Inc. MET-5013). Metabolic maps were generated by integrating the respective metabolite peaks. Regions of interest (ROIs) were drawn in the lateral cortex, with T_2-weighted proton images serving as anatomical reference.

Results: Mice receiving PTZ demonstrated gradually more severe seizure responses, whereas sham control mice showed no seizure as measured by Racine behavioral score. Maps for Pyr, Lac, and Lac-to-Pyr ratio from representative control and PTZ animals in Fig.1a show elevated Pyr-to-Lac conversion in the lateral cortex of PTZ mice. PTZ-administrated animals showed significant elevations in Pyr-to-Lac conversion compared to controls (1.96±0.5 vs 1.63±0.41, p=0.03, Fig. 1.b). Similarly, significantly elevated extracellular Lac concentrations were detected using the lactate assay in the brains of PTZ kindled mice compared to sham controls (7.99±3.19 vs 5.86±0.39, p=0.041, Fig. 1c). There was a significant correlation between the lactate assay and Lac-to-Pyr ratio (R^2=0.4299, p<0.001). We checked blood-brain barrier (BBB) integrity after PTZ kindling using gadolinium-based MRI. No significant differences (p=0.3778) in pre/post gadolinium signals T_1w MRI, suggest ^{13}C HP Pyr transport across the BBB, a rate-limiting step in the conversion of Pyr to Lac, was likely unaffected by PTZ.

Conclusions: This study demonstrates that MRSI of HP [1-^{13}C]Pyr can identify elevated Pyr-to-Lac conversion in a PTZ mouse model of epilepsy with the MR metric correlating with *ex vivo* extracellular Lac. These findings indicate the potential of HP MRSI as a clinical tool for identifying the EF.

Acknowledgments: This work was supported by NIH grants R21 DK131357, R21 NS133531, and R21 NS139180.

References:

1. Dufour F, Koning E, Nehlig A. Experimental neurology. 2003;182(2):346-52.
2. Hill RA, Chiappa KH, Huang-Hellinger F, Jenkins BG. Epilepsia. 1999;40(7):912-20.
3. Mayer D, Yen YF, Tropp J, Pfefferbaum A, et al. Magn Reson Med. 2009;62(3):557-64.
4. Larson PE, Kerr AB, Chen AP, Lustig MS, et al. J Magn Reson. 2008;194(1):121-7

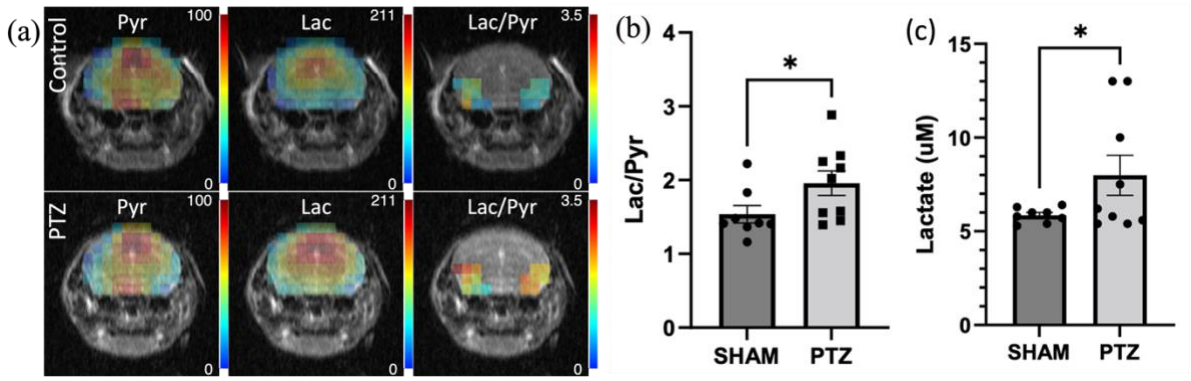

Figure 1. (a) Metabolic images (FOV = 32x32 mm^2, 4-mm slice) of Pyr, Lac and Lac/Pyr acquired from control (top) and PTZ (bottom) animals are superimposed onto the proton MRI. For each animal, the metabolite intensities are normalized to maximum in the respective Pyr map. Lac/Pyr images show the magnitude of the Lac-to-Pyr ratios. PTZ animals show higher Lac/Pyr in the lateral cortex than control animals. **(b)** Average Lac-to-Pyr ratio measured from dynamic 3D MRSI in lateral cortex ROIs of the brain in sham control (n=8) and PTZ mice (n= 9) (p= 0.03). **(c)** Average extracellular lactate concentrations measured with lactate assay kit in PTZ vs sham animals (p= 0.041).

Imaging Guidance Improves Cell Transplantation Efficacy for Tracking Cellular Dynamics Under 2-Photon Intravital Microscopy

Jinghui Wang, Miroslaw Janowski, Piotr Walczak and Yajie Liang

Department of Diagnostic Radiology and Nuclear Medicine, University of Maryland School of Medicine, Baltimore, MD. Corresponding author: Yajie.liang@som.umaryland.edu

Background

Neural stem cell transplantation has been widely pursued to treat stroke, trauma, or neurodegenerative diseases. Optimizing delivery procedures to the mouse cerebral cortex is critical for accurate and efficient manipulation of neural circuits in neuroscience research. Furthermore, intravital imaging is urgently needed to elucidate the post-transplantation behavior of transplanted cells in the host with high spatial and temporal resolution.

Objective

This study aims to test whether the pulse-elevation mode of cell delivery could significantly enhance cell loading efficiency and establish the single-cell tracking platform under 2-photon microscopy.

Methods

Mouse neural stem cells (C17.2 cells) stably expressing the fluorescent protein mVenus or mCherry through transduction with lentiviral vector FCIV or mCherry-H2BGCaMP6s were injected at the concentration of 2.5×10^4 cells/μl to 0.6 % low-melting agarose [1] or the mouse brain at the coordinate of AP -3.35 mm, ML 1.75 mm using stereotaxic equipment. Before injection, the needle (100 μm diameter glass pipette) was extended to 700 μm and then retracted to a target depth of 500 μm in both pulse-elevation and non-stop modes. Infusion settings for pulse-elevation mode: step1: rate: 0.1 μL/min, 20 nL; delay 20 s and withdraw to 0.4 μm; step2: rate: 0.1 μL /min, 20 nL; delay 20 s and withdraw to 0.3 μm; step3: rate: 0.1 μL /min, 20 nL; delay 20 s and withdraw to 0.2 μm. Non-stop mode used the same rate without withdrawal or delay steps. For *in vitro* experiments, fluorescent images were taken under Leica DMi8. For the *in vivo* experiment, a cranial window was made for cell transplantation, followed by the installation of a coverslip. Two-photon imaging was performed on day 3 post-transplantation every 12 hours for 3 days [2].

Results

In the *in vitro* experiment, we found that the pulse-elevation mode could accommodate more cells than the non-stop mode (Figure 1a). In vivo, using the same infusion procedure, we observed a clear needle track post-transplantation on day 0, and cells were confined to it (**Figure 1c).** These observations suggest that the pulsed-elevation mode can precisely deliver and hold cells within the needle track and improve cell loading efficiency.

For single-cell tracking, 2-photon imaging was performed on post-transplantation day 3 and every 12 hours for 3 days. We successfully tracked the migration trajectories of single cells for 3

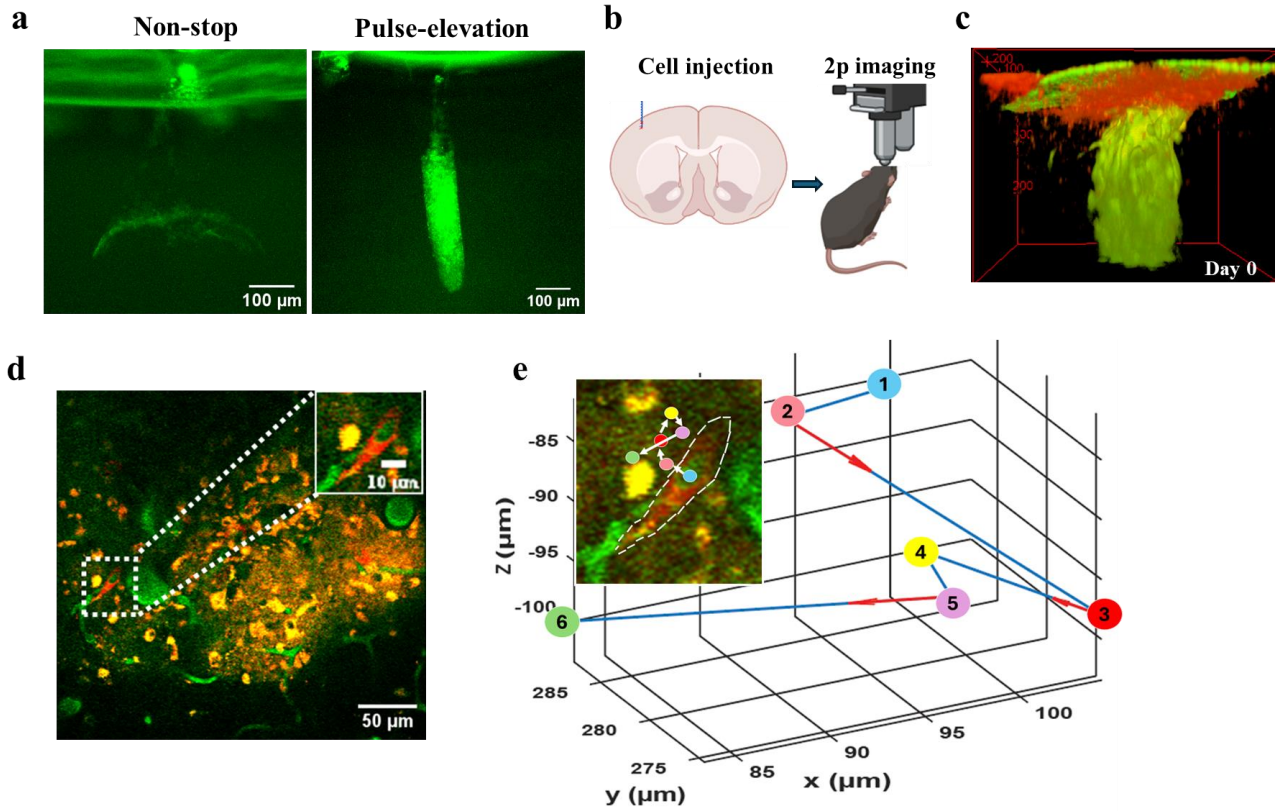

Figure 1 (**a**) Design of in vitro experiments and images of needle tracks under a Leica microscope; (**b**) Design of in vivo experiment; (**c**) 3D view of the imaging stack showing transplanted cells in needle track on day 0. Scale bar in (**a**), 100 μm. (**d**) Transplanted cell under 2-photon microscopy; (**e**) Cell trajectory diagram; (**f**) Trajectory spatial diagram of tracked cell. Scale bar in (**d**), 50 μm; Scale bar in (e), 10 μm. Red: target cell, green: blood vessel.

days **(Figure 1d).** By analyzing the position data, we can obtain the cells' planar and spatial movement trajectories **(Figure 1e).** These data help understand cells' behavior and migration patterns in the new environment after transplantation.

Conclusions

We established a platform for optical imaging-guided cell transplantation into the cerebral cortex of mice and for intravital cell tracking. Through *in vitro* and *in vivo* experiments, we found that the pulse-elevation injection method can significantly increase the efficacy of cell transplantation and improve cell loading efficiency. Through 2-photon imaging, the data we collected can help understand cells' behavior and migration patterns in their new environment after transplantation. Further evaluation of this preliminary conclusion is needed.

Reference

1. Chen ZJ, Gillies GT, Broaddus WC, Prabhu SS, Fillmore H, Mitchell RM, Corwin FD, Fatouros PP. *A realistic brain tissue phantom for intraparenchymal infusion studies.* J Neurosurg. 2004 Aug;101(2):314-22. doi: 10.3171/jns.2004.101.2.0314. PMID: 15309925.
2. Liang Y, Walczak P. *Long term intravital single cell tracking under multiphoton microscopy.* J Neurosci Methods. 2021 Feb 1;349:109042. doi: 10.1016/j.jneumeth.2020.109042. Epub 2020 Dec 16. PMID: 33340557.

Engineering Glial Progenitor Cells to Facilitate P2x7 Receptor Blockade as a Therapeutic Strategy for Addressing Acute Inflammation Resulting from Traumatic Brain Injury

Lucia Fadon Padilla[1] PhD, Guanda Qiao[1] MD, PhD, Lukasz Kalkowski[1] PhD, Lorissa McDougall[1], Chengyan Chu[1] MD, Miroslaw Janowski[1] MD, PhD, Piotr Walczak[1] MD, PhD

[1]Department of Diagnostic Radiology and Nuclear Medicine, University of Maryland School of Medicine, Baltimore, MD.

Background: Traumatic brain injury (TBI) is a prevalent and debilitating condition. Inflammatory processes contribute significantly to both primary and secondary brain damage. "Danger signals" are potent activators of local immune responses, thereby mediating secondary brain damage—particularly ATP and its P2x7 receptor are attractive targets for therapy. In order to test our therapy to combat this harmful inflammation, there is a need for a rodent model that resembles the human underlying pathology.

Objective: We propose a therapeutic approach to combat acute inflammation after TBI using engineered glial-restricted precursor (GRP). We also aim to develop a model that resembles clinical features as a basis for testing our therapy.

Methods: *In vitro*: GRP cells were transfected with bicistronic mRNA encoding both a HaloTag marker and P2x7-blocking nanobody. Transfection efficiency was evaluated using flow cytometry. *In vivo*: We initiated this phase by characterizing the effects of intraarterial administration of GRPs directly to the brain, assessing safety in healthy animals. Subsequently, we induced TBI in mice using a controlled cortical impact (CCI) model, characterized the lesion, and administered GRPs intraarterially under MRI guidance. GRP accumulation in the brain was measured by bioluminescence. We then tested utility of a closed head injury (CHI) model by performing escalation of the severity of injury by applying 1-3 impacts using CCI device 2mm displacement and the speed of 3 m/s. The injury was analyzed by behavioral tests and MRI.

Results: We successfully achieved an approximately 50% transfection efficiency following mRNA-P2x7 transfection (Fig.1A). Intra-arterial administration of GRPs in healthy mice was safe. The CCI TBI model produced noticeable cortical lesions visible on T2w MRI (Fig.1B). Furthermore, intra-arterial injection caused GRP accumulation in the ipsilateral hemisphere of the brain (Fig. 1C). However, brain tissue loss in the region in direct contact with the impactor was also noticed with this model. Therefore, we tested a CHI model and evidenced neurological impairment, opening of the blood-brain barrier with preservation of tissue structure, and some inflammation, laying the groundwork for testing our therapy.

Conclusions: We demonstrated the feasibility of GRP-based immunomodulation targeting the P2x7 receptor. Our next steps involve testing our therapy in a repetitive CHI model.

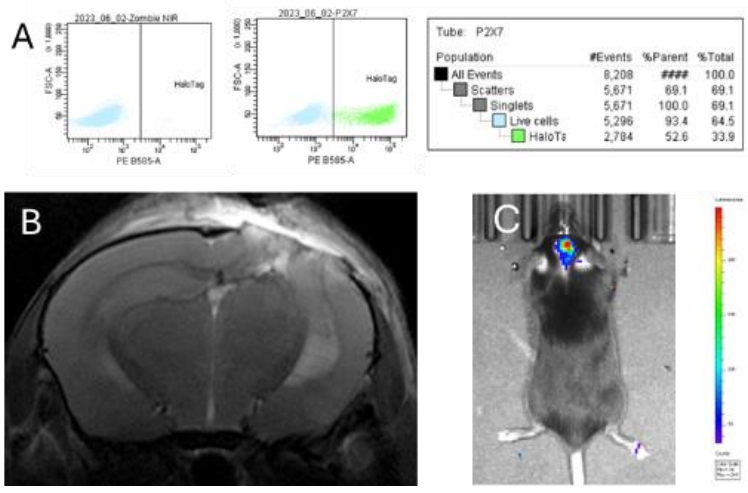

(A) Representative flow cytometry dot plots of GRPs at 24 h after mRNA P2X7 transfection. (B) Prominent cortical lesion is visible one month after induction of CCI as hyperintense signal on T2w MRI. (C) Bioluminescence signal shows brain accumulation of GRPs in the brain after intra-arterial administration.

Transplanting “Drug Factories” Human Mesenchymal Stem Cells for Adjuvant Therapy of Stroke

Lukasz Kalkowski, PhD[1]; Guanda Qiao, MD, PhD[1]; Yajie Liang, PhD[1]; Miroslaw Janowski, MD, PhD[1,2]; Piotr Walczak, MD, PhD[1]

1 Department of Diagnostic Radiology and Nuclear Medicine, University of Maryland School of Medicine, Baltimore, MD, USA;

2 UM Greenebaum Comprehensive Cancer Center, University of Maryland School of Medicine, Baltimore, MD, USA;

Background: Stroke ranks among the leading causes of death and disability, and modulating excessive inflammatory responses during the acute phase can be an effective adjuvant treatment. The danger-associated molecular pattern (DAMP)-related receptor P2x7 is a critical therapeutic target. However, poor brain accumulation of systemically injected antibodies is a major obstacle to exploiting this strategy. Our hypothesis states that mRNA-transfected mesenchymal stem cells, engineered for the transient production of anti-P2x7 nanobodies, will result in a swift onset and sustained accessibility of P2x7 nanobodies throughout the stroke area.

Objective: We aim to use hMSC for transient *in situ* production of P2x7-blocking nanobodies. We propose this strategy as an adjuvant therapy to ameliorate post-stroke neuroinflammation.

Methods: A construct (13A7-HaloTag_Myc_His) expressing anti-P2x7 nanobody (with post-translational dimerization) with HaloTag, HisTag and myc-tag was used. Human MSCs were transfected using either DNA or mRNA. Using flow imaging, we quantified positive cells and transfection efficiency dynamics by means of JF549 HaloTag ligand fluorescence. Western blot was used for the detection of specific antigens (myc-tag) in the cell media either 1- and 3-days post-transfection. The functionality of the produced nanobody was assessed using Fluo-4 (calcium-specific fluorescence) assay, adding P2x7 ligand (bzATP) to P2x7-expressing HEK293 cells. For animal studies, adult male mice underwent tMCAO and immediate intraarterial transplantation of transfected hMSCs, labeled with SPIOs (Molday ION™ EverGreen) and HaloTag ligand (JF549) for MRI and histology detection, respectively. Animals were euthanized at day 1 and week 1 post-MCAO/tx and histological assessment was performed.

Results: After one day, the transfection efficiency of mRNA was significantly higher (A) compared to plasmid transfection. We have confirmed the presence of the nanobodies in the media both 1 day and 3 days post-transfection by Western blot (B), confirming the release of the complete nanobodies into the cellular media. Nanobodies are proved to be functional by blocking P2x7-dependent Ca^{2+} influx into the cytoplasm (C) as indicated by the Fluo-4 calcium binding assay. When transplanted into MCAO mice, they reside within the ipsilateral hemisphere for as long as one week (D) and are detected in the tissue after both one day and one week (E).

Conclusions: We have successfully demonstrated the feasibility of using hMSCs as “drug factories” to block the P2x7 receptor with high efficiency. The cells can produce functional nanobodies both *in vitro* and *in situ* post-transplantation.

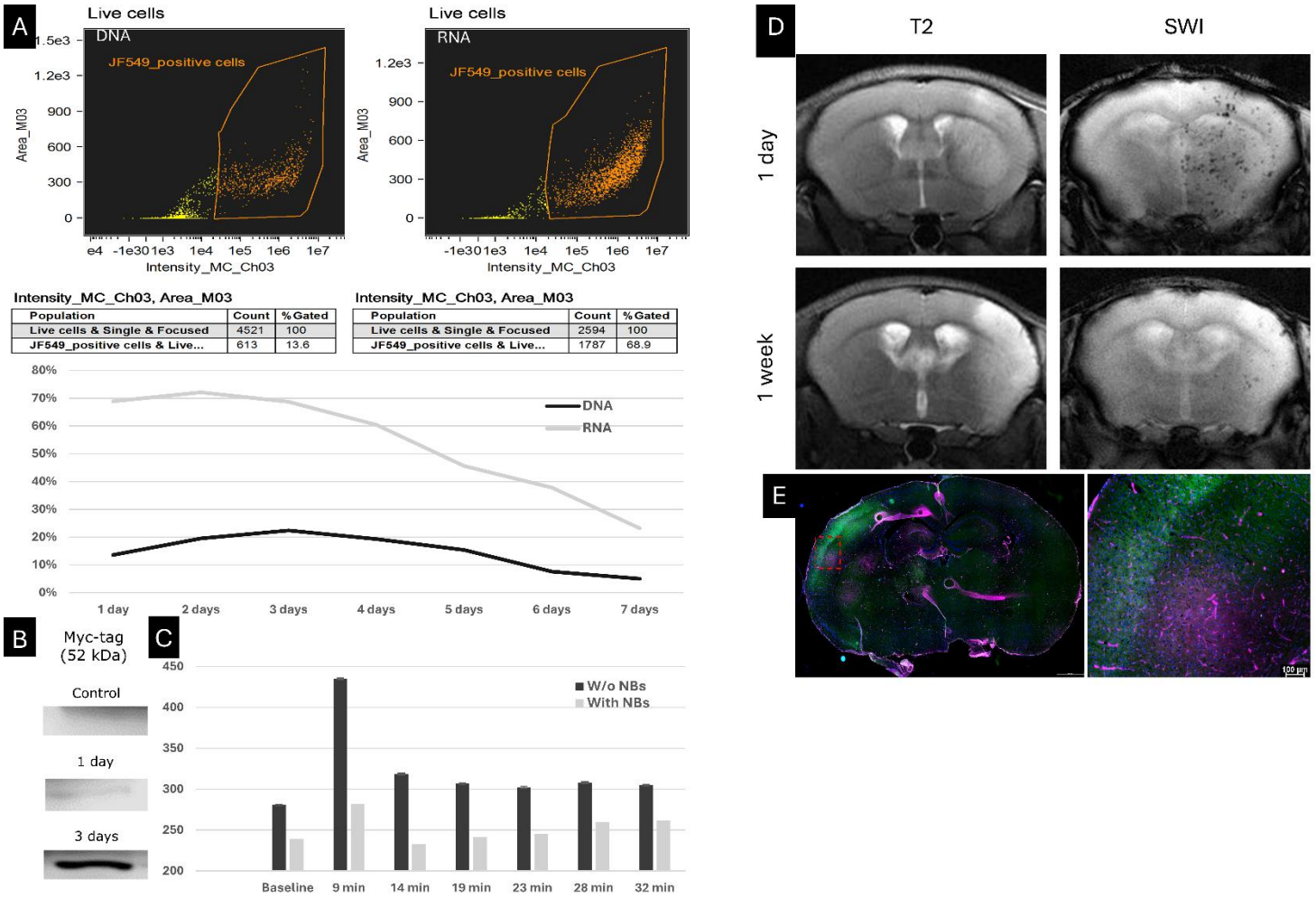

Figure 1. Human MSC transfection assessment using 13A7-HaloTag_Myc_His construct (A): Flow imaging graphs for transfection efficiency for either DNA and RNA with respective positive cell numbers in different time points. Anti-myc-tag Western blot analysis of transfected cells media (B). Calcium release assay results (overall fluorescence) after adding the cell media with or without nanobodies (NBs) into P2x7-positive HEK cells (C). MRI coronal T2 (left) and SWI (right) both one day and one week after MCAO/transplantation of SPIO- labeled hMSC (D). Cells are detected in histology one day post-MCAO/tx using EverGreen (SPIO-specific fluorophore; green) and Stem121 (human cell cytoplasm marker; magenta) as transplanted cells-specific labels (E).

Enhanced sensitivity of downfield MRSI at 7T

İpek Özdemir Ph.D.[1], Semra Etyemez M.D.[2], and Peter B. Barker, D.Phil. [1,3]

[1]Russell H. Morgan Department of Radiology and Radiological Science, The Johns Hopkins University School of Medicine, Baltimore, MD, [2]Department of Psychiatry, Obstetrics & Gynecology, Weil Cornell Medicine, New York, NY; [3]F. M. Kirby Research Center for Functional Brain Imaging, Kennedy Krieger Institute, Baltimore, MD

Background: Downfield (DF) proton magnetic resonance spectroscopic imaging (MRSI) of exchangeable protons is expected to have superior sensitivity at high magnet field strengths.

Objective: To quantitatively compare signal-to-noise ratios (SNR) and Cramer-Rao Lower Bounds (CRLB) for amide resonances in the human brain measured at 3 and 7T using closely DF-MRSI matched protocols.

Methods: 5 normal volunteers (25-52 yrs, 4F) were imaged using Philips 3T "Elition" and 7T "Achieva" scanners. Both systems have 32-channel receive head coils and 16-channel local shim arrays (MRShim GmbH), in addition to high order spherical harmonic shims.

3D DF-MRSI data were collected using a previously developed pulse sequence with spectral-spatial excitation and frequency selective refocusing pulses [1-3]. Scan parameters on both systems were 200×180×120 mm FOV, 29×26×8 matrix size, 1 excitation, 1.5X SENSE acceleration, scan time 10.6 min. TR/TE(ms)/flip angle were 282/24/61° at 3T and 222/13/55° at 7T. In addition, 3D FID-MRSI unsuppressed H_2O scans were also collected at the same spatial resolution. An automated processing pipeline generated amide maps, SNR, and CRLB values from LCModel analysis. 7 brain regions were selected for analysis; amide (≈ 8.1 to 8.3 ppm) SNR and CRLB values (%) were compared between 3 and 7T data using paired t-test.

Fig. 1. (A) 3T 7T

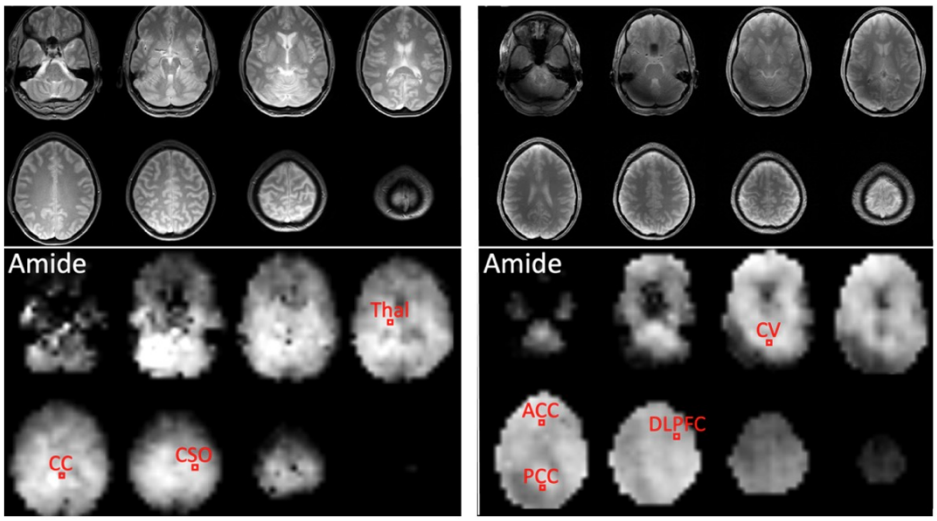

(B) 3T / 7T

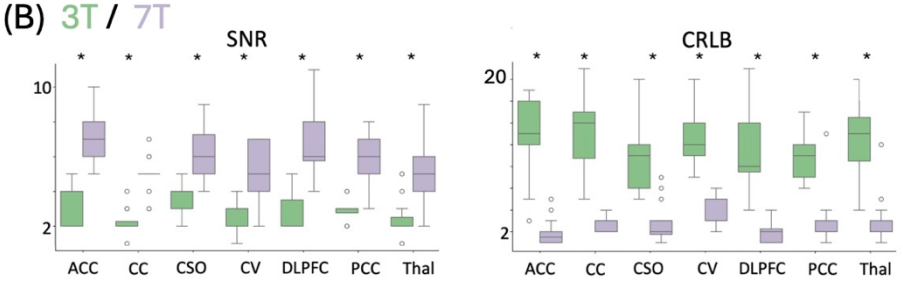

Results: Fig. 1A shows localizer proton density MRI and amide images from one subject at both 3 and 7T, and 1B shows regional SNR and CRLB values. Significantly increased amide SNR and decreased CRLB values (* *p<0.001*) were found at 7T. Averaged over all brain regions, SNR was 2.5±1.1/5.9±1.8 (3T/7T), and CRLBs 15.2±9.2/4.7±1.6. 7T MRI and amide images did show some regional signal drop-off due to transmit B_1 inhomogeneity, however.

Conclusions: 3D DF-MRSI at 7T showed more than double SNR and three-fold less CRLB values compared to 3T, confirming the expected improvements at higher field. Improvements are probably due to multiple factors, including higher magnetization at 7T, the shorter minimum TE available, less relative line-broadening due to chemical exchange, and more favorable SENSE g-factor, amongst others.

References

1. Považan et al. MRM 2022;87:1661-72
2. Özdemir et al. MRM 2023;90:814-22
3. Özdemir et al. MRM 2024;92:890-99

Open-source analysis of magnetic resonance spectroscopic imaging (MRSI) data in Osprey

Helge J. Zöllner[1], PhD; Dillip K. Senapati[1], PhD; İpek Özdemir[1], PhD; Doris D.M. Lin[1], MD; Georg Oeltzschner[1], PhD; Peter B. Barker[1,2], PhD

[1]Russell H. Morgan Department of Radiology and Radiological Science, The Johns Hopkins University School of Medicine, Baltimore, MD, United States; [2]F. M. Kirby Research Center for Functional Brain Imaging, Kennedy Krieger Institute, Baltimore, MD, United States

Background: Magnetic resonance spectroscopic imaging (MRSI) is a versatile technique to investigate *in vivo* metabolism[1]. However, MRSI data processing is a demanding task, and only a few software packages support end-to-end analysis of MRSI data[2].

Objective: To implement MRSI data analysis into Osprey[3], an open-source ^{1}H-MRS software package including pre-processing, linear-combination modeling, tissue correction, and quantification, adhering to recent consensus guidelines[4].

Methods: Software implementation: Osprey is a ^{1}H-MRS analysis package that currently offers end-to-end analysis of single voxel MRS data from all major vendors. Each of Osprey's native modules was modified to support MRSI data. *OspreyLoad*: Loads vendor native MRSI raw data formats from Philips (.data/.list; .spar/.sdat) and Siemens (.rda), as well as NIfTI-MRS, a new community standard[5].Coil-combination, retrospective motion compensation[6], and spatial transformation are performed (depending on the input data format). *OspreyProcess*: Performs frequency correction and removal of the residual water signal using a HSVD filter[7]. If needed, difference spectra from edited experiments are generated. *OspreyFit:* Linear-combination modeling (LCM) is used for metabolite estimation. The implemented LCM algorithm[8] is versatile and easy to modify for adaptation/exploration of new modeling approaches. *OspreyCoreg/Seg:* If available, the MRSI data are co-registered to a structural T_1-weighted image, and the tissue composition (gray/white matter and cerebrospinal fluid) of each MRSI voxel is calculated using SPM12 segmentation. *OspreyQuantify*: Metabolic maps are computed for all estimated metabolites. If no water MRSI scan is provided, creatine-referenced metabolic maps are generated. Otherwise, water-referenced estimates with and without tissue-specific relaxation correction are generated. The results from all analysis steps, including the processed spectra, LCM results, tissue compositions, and metabolic maps, are exported in NIfTI-MRS format. Visualization: The NIfTI-MRS format allows for easy visualization and inspection of all results, for example, in *FSLeyes*. Other NIfTI data from any image modality can be conveniently overlayed. Application: An example Philips dataset (Philips 3T Ingenia Elition, 32-channel head coil; 22 years old female healthy volunteer), including short-TE and GABA-edited spin-echo multi-slice MRSI and water reference MRSI data, was analyzed to demonstrate Osprey's capabilities. The spin-echo edited-MRSI sequence used hypergeometric dual-band (HGDB) water and lipid suppression pulses and 8 outer-volume suppression (OVS) pulses[9]. All MRSI scans were performed with three 15-mm oblique-axial slices (2.5 mm gap), 14x17 matrix (elliptical k-space sampling), and nominal voxel size 12×12×15 mm (≈ 2.2 cm^3). For GABA-editing, sequence parameters were TR/TE = 1.8 s / 68 ms, 4 excitations (2 edit ON, 2 edit OFF), edit ON/OFF frequencies 1.9/0.7 ppm, editing pulse bandwidth 150 Hz ('sg150'), scan time 22:21 min. The short-TE spin-echo MRSI parameters were TR/TE = 1.75 s / 20 ms, 1 excitation, scan time 5:50 min. Parameters for water MRSI were TR/TE = 0.85 s / 20 ms, 1 excitation, scan time 2:39 min. Brain coverage was from the level of the third ventricle to the vertex.

Results: The example dataset was successfully analyzed using the proposed pipeline. Figure 1 shows the results of the center slice of the MRSI data in *FSLeyes*. The left column shows the T_1-weighted anatomical images with the brain surface delineated in white and the current voxel position indicated by the green crosshair. The center column shows the LCM results of the short-TE (top) and GABA-edited (bottom) MRSI of the corresponding voxel location (data in dark blue, model in yellow, and baseline estimate in light blue; note that the difference between data and model (residual) was removed for clarity). The right column shows examples of water-referenced metabolite maps for tNAA and tCho from the short-TE MRSI and the water-referenced GABA+ metabolite map from the GABA-edited MRSI scan scaled to the concentration of pure water without tissue-specfic relaxation correction. Note that arbitrary layouts/overlays can be used in *FSLeyes*. The current implementation of Osprey is available online on GitHub (https://github.com/schorschinho/osprey/tree/MRSI).

Conclusion: MRSI data analysis and NIfTI-MRS export were successfully integrated into the open-source ^{1}H-MRS analysis package Osprey.

References:1.Maudsley 2020; 2. Clarke 2021; 3. Oeltzschner 2020;4. Near 2020; 5. Clarke 2022; 6. Chan 2019; 7. Barkhuijsen 1987; 8. Zöllner 2024; 9. Zhu 2011;

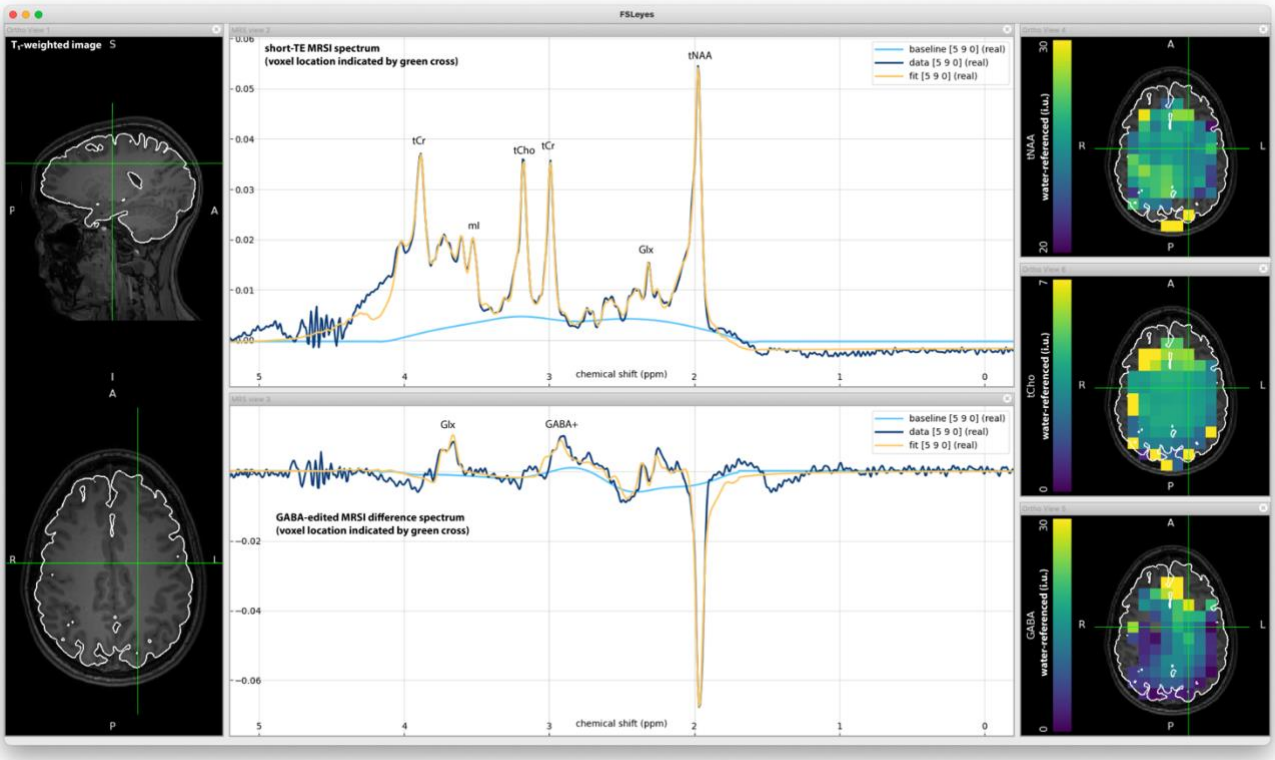

Figure 1 – Example FSLeyes visualization of MRSI data (of a 22 years old female healthy volunteer) analyzed in Osprey. The T1-weighted image is shown in the first column including the delineation of the brain surface and the current voxel position indicated by the green crosshair. The middle column shows the LCM results for the short-TE (top) and GABA-edited difference spectra (bottom) of the corresponding MRSI voxel. Example water-referenced maps for tNAA (top) and tCho (middle) from the short-TE and GABA+ from the GABA-edited difference spectrum are shown in the last column.

Radiolabeling of mesenchymal stem cells for image guidance-based precision medicine

Sharma S, Gulisashvili D, Salemdawod A, Kalkowski L, Brzezinski M, Liang Y, Walczak, P, Janowski M
Program in Image Guided Neurointerventions, Center for Advanced Imaging Research. Department of Diagnostic Radiology and Nuclear Medicine, University of Maryland, Baltimore.

Background: Mesenchymal stem cells (MSCs) are highly promising therapeutic agents. However, unknown biodistribution upon transplantation limits the understanding of their therapeutic effects. This limitation particularly affects advanced and more precise intra-arterial routes of cell delivery.
Objective: To develop and optimize the radiolabeling of MSCs to facilitate image-guided precision medicine.
Methods: The radiolabeling procedure involves chelating ^{89}Zr atoms with deferoxamine (DFO), which is then incubated with cells for 30 minutes in Eppendorf tubes. After washing, the cells are analyzed for radioactivity uptake, cell survival, and cell proliferation and metabolism as measured by CCK8 assay over a week (days 1,3, 5, 7). We used 100k MSCs per sample throughout the study, as it is a typical dose for intra-arterial delivery to the brain. Independent variables include cell concentration (10k/mL and 2k/mL), added radioactivity per sample, and radiation intensity during incubation. Radioactivity captured per cell uniquely serves as both types of variables depending on the situation. Dependent variables include radioactivity captured per cell (labeling yield), labeling efficiency, radioactivity efflux after a day and a week, cell viability, and cell proliferation and metabolism. We conducted four repetitions of the experiment, totaling 1464 data points.
Results: We observed that lower cell concentration (2k/mL) was associated with better outputs across all dependent variables. However, the condition characterized by the highest uptake radioactivity per cell and the most favorable CCK8 assay included higher cell concentration (10k/mL) **(Fig. 1a)**. As expected, adding more radioactivity and achieving higher radiation intensity allowed for better radioactivity yield per cell **(Fig. 1b)**, which led to a higher efflux of radioactivity afterward **(Fig. 1c)**. While higher radioactivity uptake per cell decreased the cell viability at the end of the radiolabeling procedure **(Fig. 1d)**, it positively affected MSC proliferation and metabolism **(Fig. 1e,f)**.
Conclusions: We have shown that lower cell concentration resulted in positive effects across all dependent variables. Higher radioactivity per cell also contributed to better cell proliferation and metabolism, obviating negative long-term consequences of radioactivity on cell well-being, even if it negatively affected cell survival during the procedure. Interestingly, we have observed accelerated growth of MSCs with high radioactivity per cell, which requires further investigation.

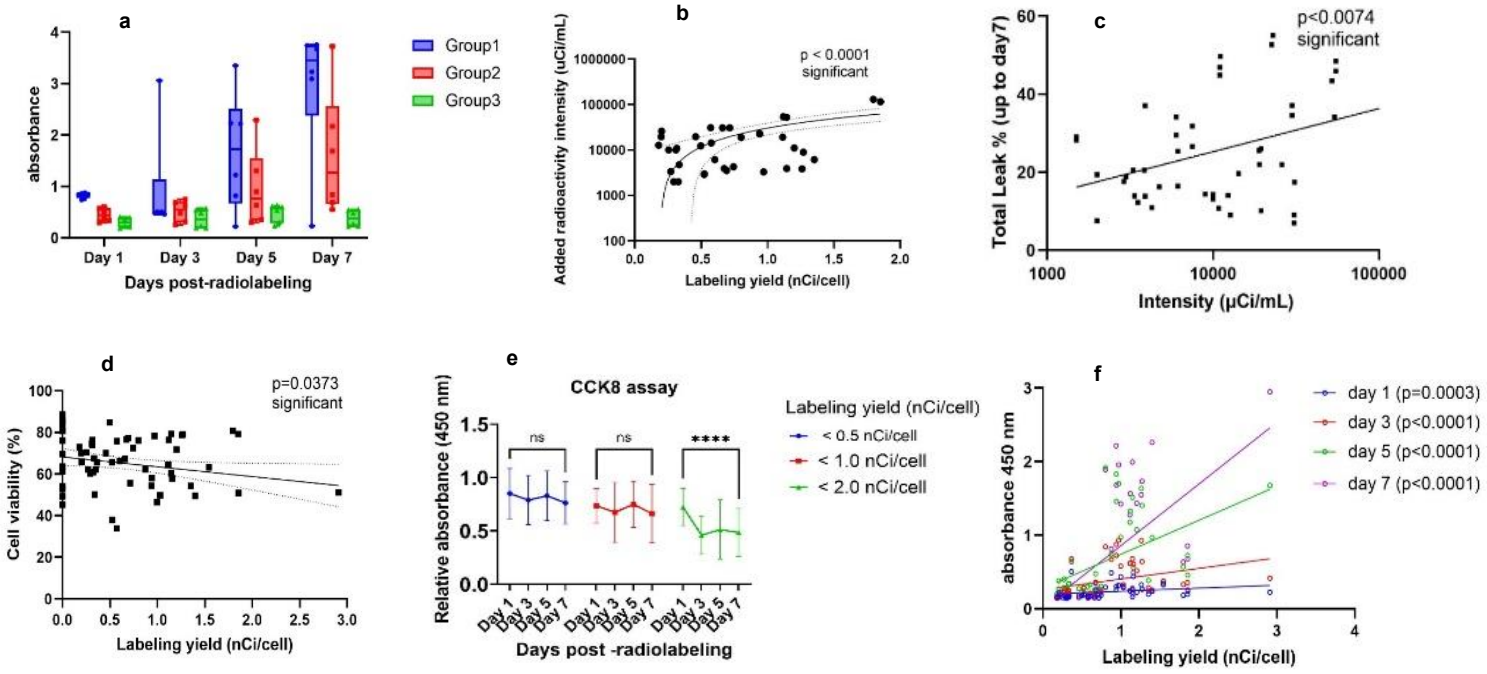

Figure 1. Mesenchymal stem cell radiolabeling analysis

CRISPR/Cas9-based base editing of tuberous sclerosis complex gene 2 to explore its roles in various pathologies

Salemdawod A[1,2], Liang Y[1], Walczak P[1], Maciaczyk J[2], Janowski M[1]

[1]University of Maryland School of Medicine, Baltimore, USA, Department of Diagnostic Radiology
[2]University Hospital Bonn, Bonn, Germany, Department of Neurosurgery

Objective: Tuberous sclerosis complex (TSC) is a genetic multisystem disorder resulting from a mutation in either the TSC1 or TSC2 gene. Most of these mutations (ca. 82%) are single nucleotide point mutations (SNP). There is growing evidence of the involvement of TSC2 mutations in various cancerous diseases. However, point mutations comprise the majority of TSC2 cases (ca. 75%). Moreover, Disruption of the TSC2 gene selectively in mesenchymal progenitors leads to extensive hamartomas, linking stem cells with this most characteristic pathological phenotype. The recent advances in CRISPR-based gene editing tools present a novel diagnostic and potentially therapeutic opportunity in TSC patients with SNP mutations. Therefore, we studied the feasibility of induction of the two most frequent TSC point mutations in mesenchymal stem cells (MSCs).

Methods: We targeted TSC2.1832 G>A (Arg611Glu) and TSC2.5024 C>T (Pro1675Leu). The CRISPR/Cas9 gRNAs were designed using (Invitrogen TrueDesign Genome Editor™), considering highest predicted editing efficiency and the least off-target edits. CRISPR/Cas9 ribonucleoprotein (RNP) was delivered through Lipofectamine-CRISPR Max transfection agent (Thermofisher): Human Embryonic Kidney 293 (HEK293) and human MSCs served as test subjects. The editing efficiency was determined using Sanger sequencing.

Results: The editing efficiency of the TSC2.1832 G>A, (Arg611Glu) mutation was higher in MSCs, with rates reaching 80% **(Fig. 1A)** in the first run and 85% **(Fig. 1B)** in the second run, compared to 73% in HEK293 cells. In contrast, the editing efficiency of TSC2.5024 C>T (Pro1675Leu) mutation was higher in HEK293 cells, at 51%, compared to 28% in MSCs in the 1st first run and 38% in the second run. Importantly, no off-target edits were observed within the PAM site.

Conclusions: Induction of the most frequent TSC-related point mutations in MSCs can be achieved at very high yield, although there are significant differences in efficiency between gRNAs. INDUCE-seq and whole-genome sequencing are inevitable in determining all off-target edits. In summary, CRISPR-based gene editing is a promising strategy for increasing understanding of the TSC2- derived pathologies.

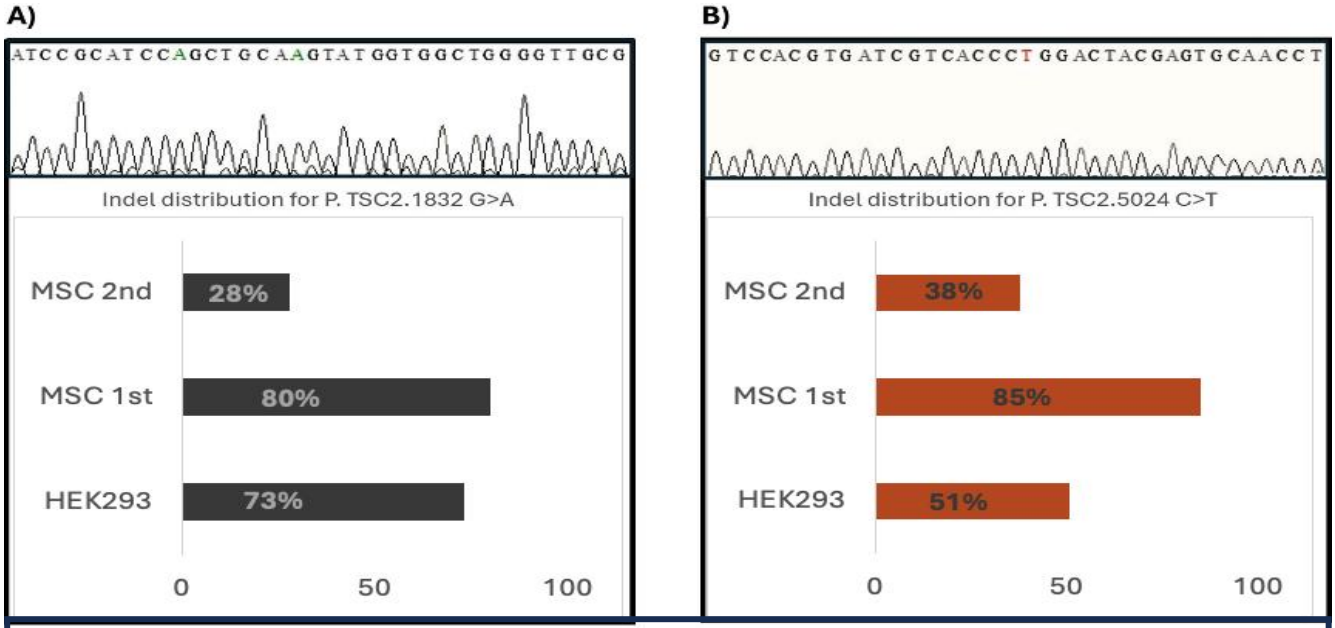

Figure 1: CRISPR/Cas9 RNP-mediated base editing in human MSCs. (A) Result of Sanger sequencing to detect editing efficiency for the first mutation in 3 different cell groups showing a high editing efficiency in HEK293 of 73% and an increasing editing efficiency in hMSCs using RNP:gRNA ratio of 1000:750 ng. The amplicon sequencing shows 2 SNP edits (G>A) at position 1832 (desired) and at position 1839 (undesired). B) Result of Sanger sequencing to detect editing efficiency for the second mutation in 3 different cell groups showing a significantly lower efficiency in HEK293 of 51% and a decreasing editing efficiency in hMSCs, despite using the same transfection conditions and a RNP:gRNA ratio of 1000:750 ng. There were no undesired edits detected within the sequenced amplicon.

Functional Gradient Analysis for the study of Alzheimer's Disease

ALDO CAMARGO,[1], AND ZE WANG[1]

Abstract:

Background: Dys-connectivity has been repeatedly shown in Alzheimer's Disease (AD) but the change of connectivity gradient across the brain is under-studied. In this study, we used resting state fMRI (rsfMRI) from the Alzheimer's Disease Neuroimaging Initiative (ADNI) to build a whole brain functional connectivity matrix. We then compared the major connectivity gradients decomposed from the connectivity matrix from normal controls (NC), mild cognitive impairment (MCI), and AD patients.

Methods: 40 NC, 38 MCI, and 40 AD were included in the analysis. Data preprocessing including motion correction, slice time correction, normalization, and artifact component removal, was performed using SPM12 and FSL. Mean rsfMRI time series was extracted from each of the 400 segments in the Schaefer atlas. A 300x300 functional connectivity matrix was calculated for each subject. Connectivity gradients were subsequently calculated using the BrainSpace toolbox. A mean connectivity matrix and its gradients were calculated for NC, MCI, and AD separately. Individual subject's gradients were then aligned to those population level ones and compared across groups through two-sample t-test. Our analysis limits to the first three gradients as the corresponding eigenvalues explained >80 % (See Figure 1). Multiple comparison correction was performed using Bonferroni correction. Additionally we compared differente machine learning models to classify NC, MCI, and AD based on the features: gradients, age, and gender. We also generated 1000 Boostrapping samples to check if the results have the same pattern.

Results: Figure 2 shows the first gradient map for each sub-group. The gradients were lowest in occipital cortex, and increased in the motor network and temporal cortex, and then gradually went down toward prefrontal cortex. Figures 3-5 are the statistical comparison results. The first gradient map showed the largest cross-sectional changes. Compared to NC, MCI had reduced gradients in occipital cortex, motor cortex, and temporal cortex. Gradients in occipital cortex and posterior part of temporal cortex further reduced in AD compared to MCI, and AD patient showed gradient reduction in prefrontal cortex; and a reduction of the gradients in the prefrontal cortex is observed when comparing NC with AD groups.

Conclusion: We found consistent functional connectivity gradient reduction in the AD continuum in occipital cortex and temporal cortex, suggesting a common pathway of AD-related impairment to functional connectivity. Gradient reduction was identified in motor cortex in MCI compared to NC and was found in prefrontal cortex in AD compared to MCI, and in NC compared to AD, likely related to the escalated cognitive control, and working memory decline in AD.

Key words: Functional connectivity, gradients, dementia, Alzheimer's disease.

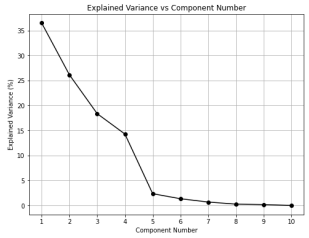

Fig. 1. Procrustes crben gradient alignment for NC, MCI and AD subjects

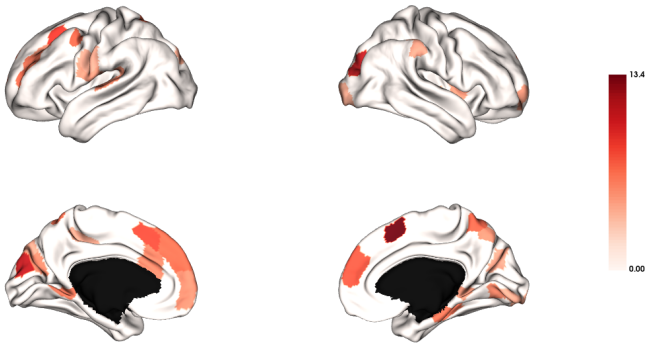

(a) NC - MCI

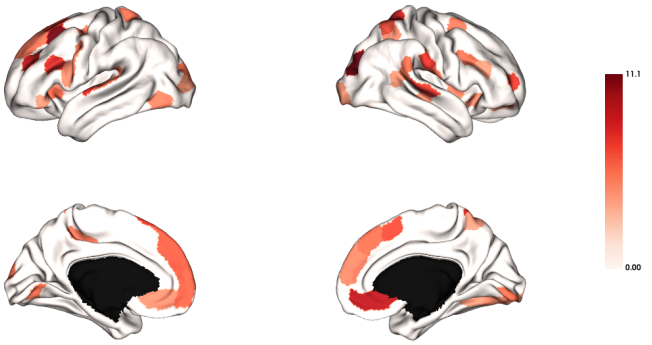

(b) MCI - AD

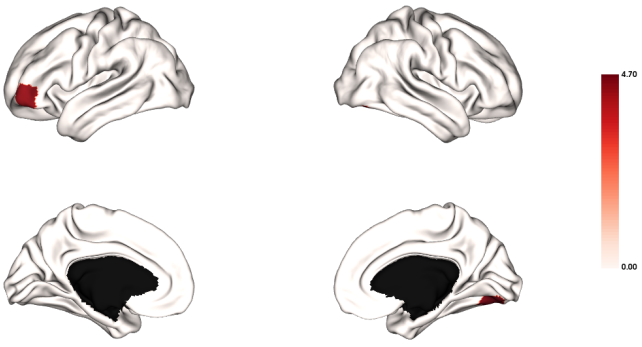

(c) NC - AD

Fig. 2. Two Sample t-test for a) NC - MCI, b) MCI - AD, and c) NC - AD. The figures show the significant t-values that correspond to the p-values corrected for multiple comparison using Bonferroni Correction. The gradients were normalized using z-transform, and the model considers the effect of age and gender

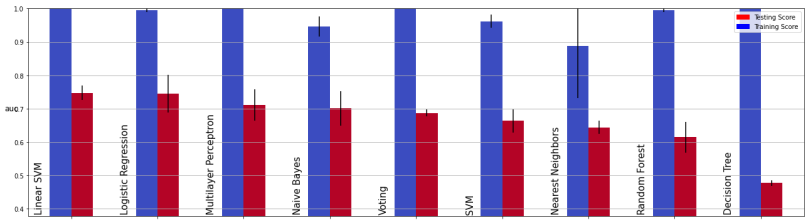

(a) Report of the AUC for the classification of NC, MCI, and AD group using the functional gradients and the MMSE score using total of 119 participants: 41 NC, 38 MCI, and 40 AD

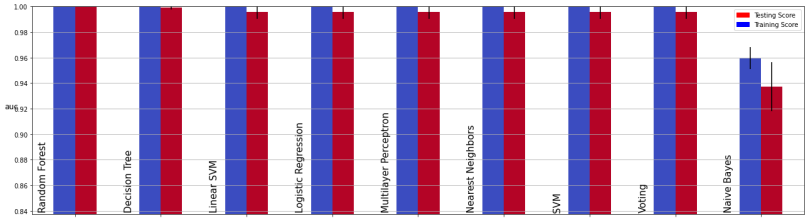

(b) Report of the AUC for the classification of NC, MCI, and AD group using the functional gradients and the MMSE score using total 1000 samples bootstrapped created

Fig. 3. a) Report of the AUC for diiffrent classifiers: Linear SVM, Logistic Regression, Multilayer Perceptron, Voting, SVM, Nearest Neighbors, Random Forest and Decision Tree using the 119 participants. b) Sames as a) but using 1000 samples boosrtrapped generated